

Improving Damped Random Walk parameters for SDSS Stripe 82 Quasars with Pan-STARRS1

KRZYSZTOF L. SUBERLAK,¹ ŽELJKO IVEZIĆ,¹ AND CHELSEA MACLEOD²

¹*Department of Astronomy
University of Washington
Seattle, WA 98195, USA*

²*Harvard Smithsonian Center for Astrophysics
60 Garden St, Cambridge, MA 02138, USA*

(Received January 1, 2019; Revised January 17, 2019; Accepted February 1, 2019)

Submitted to ApJ

ABSTRACT

We use the Panoramic Survey Telescope and Rapid Response System 1 Survey (Pan-STARRS1, PS1) data to extend the Sloan Digital Sky Survey (SDSS) Stripe 82 quasar light curves. Combining PS1 and SDSS light curves provides 15 years baseline for 9248 quasars - 5 years longer than prior studies that used only SDSS. We fit the light curves with Damped Random Walk (DRW) model, and correlate the DRW model parameters - asymptotic variability amplitude SF_∞ , and characteristic timescale τ , with quasar physical properties - black hole mass, bolometric luminosity, and redshift. We find that longer baseline allows to better constrain DRW parameters - adding PS1 data the characteristic timescale τ is a stronger function of quasar luminosity, and has a weaker dependence on the black hole mass. The variability amplitude dependence on the quasar luminosity is weaker. We make predictions for the fidelity of DRW model parameter retrieval with ZTF and LSST data.

1. INTRODUCTION

Quasars are variable at the asymptotic rms level of about 0.2 mag. They are distant active galactic nuclei, harboring a supermassive black hole surrounded by a hot accretion disk. Although it is agreed upon that the thermal emission from the accretion disk is the source of the majority of optical light, the detailed origin of variability has been debated for the past 50 years (Sun et al. 2018 and references therein). Some favor a thermal origin of variability (Kelly et al. 2013), related to the propagation of inhomogeneities ("hot spots") in the disk (Dexter & Agol 2011; Cai et al. 2016), others suggested magnetically elevated disks (Dexter & Begelman 2019), or X-ray reprocessing (Kubota & Done 2018). Indeed, it may well be that the answer involves combination of these - as Sánchez-Sáez et al. (2018) suggests, perhaps short-term variability (hours-days) is linked to the changes in X-ray flux, while long-term variability (months-years) is more intrinsic to the disk (Edelson et al. 2015; Lira et al. 2015). Nevertheless, quasar light curves have been

successfully described using the Damped Random Walk (DRW) model (Kelly et al. 2009; MacLeod et al. 2010; Kozłowski et al. 2010; Zu et al. 2011; Kasliwal et al. 2015), and the DRW parameters have been linked to the physical quasar properties (MacLeod et al. 2010, hereafter M10).

Variability is also a classification tool, allowing to distinguish quasars from other variable sources that do not exhibit a stochastic variability pattern (MacLeod et al. 2011). This property is especially useful for selecting quasars in the intermediate redshift range, which overlaps the stellar locus in color-color diagrams (Sesar et al. 2007; Yang et al. 2017)). Variability has also been used to increase the completeness in measurements of Quasar Luminosity Function (see Ross et al. 2013; Palanque-Delabrouille et al. 2013; AlSayyad 2016; McGreer et al. 2013, 2018).

Quasar, or more broadly speaking - AGN variability, has been successfully described by the broken power spectral density of the form $\log(P(f)) \propto \alpha_h \log(f)$ at high frequencies (short timescales), and $\log(P(f)) \propto \alpha_l \log(f)$ at low frequencies (long timescales). For a pure DRW process, $\alpha_h = -2$ and $\alpha_l = 0$, so that:

$$P(f) = \frac{4\sigma^2\tau}{1 + (2\pi\tau f)^2} \quad (1)$$

(with $\sigma = \text{SF}_\infty/\sqrt{2}$, τ the characteristic timescale, f the frequency), so that $P(f) \propto f^{-2}$ at high frequencies $f > (2\pi\tau)^{-1}$, and levels to a constant value at lower frequencies (Kelly et al. 2014).

There is a debate in the literature about the exact shape of the quasar PSD, and of any possible departures from the pure DRW model. Studies using quasar data from wide-field photometric surveys (OGLE, SDSS, PS1) benefit from relatively long baselines (several years), which lends focus to the low frequency part of the PSD. Overall, there is no evidence of a significant departure from DRW at long timescales (low frequencies), so that $\alpha_l \approx 0$ (Zu et al. 2013; Simm et al. 2016; Kozłowski 2016; Caplar et al. 2017; Guo et al. 2017; Sun et al. 2018). However, these ground-based surveys suffer from a sparse sampling, which can be remedied by using a space-based telescope that can carry out near-continuous observations, like the Kepler mission (Borucki et al. 2010). Studies using Kepler data, that focused on a smaller number of well-sampled AGN, with short baselines (hundred days), also did not find convincing evidence of a departure of the AGN PSD from the DRW at high frequencies, so that indeed $\alpha_h \approx -2$ (Mushotzky et al. 2011; Edelson et al. 2014; Smith et al. 2018; Aranzana et al. 2018). Since this work is based on extending the SDSS light curves (studied by M10) with the PS1 data, we directly compare the results to M10. Therefore we elect to describe the quasar PSD by the DRW, to also allow better comparison of our results with M10.

Due to its stochastic nature, the DRW process requires the light curve to be several times longer than the characteristic timescale for an unbiased parameter retrieval (Kozłowski et al. 2010; Kozłowski, Szymon 2017, hereafter K17). This means that DRW parameters recovered for short (compared to the recovered timescale) light curves may be biased, which in turn affects the correlations with physical parameters (black hole mass, Eddington ratio, absolute luminosity).

For this reason, while some studies have restricted the probed redshift range, limiting the quasar sample to where one would expect only shorter timescales based on previous studies (Sun et al. 2018; Guo et al. 2017; Kelly et al. 2013; Simm et al. 2016), some have elected not to study timescales at all (Sun et al. 2018; Sánchez-Sáez et al. 2018), or use the timescales recovered from short light curves primarily for classification (Hernitschek et al. 2016).

By extending available quasar light curves, we are able here to better recover a wider range of DRW timescales, and probe a wider range of redshifts and black hole masses. Since almost a decade ago, when M10 published their study based on SDSS Stripe 82 data, new datasets (PS1, PTF, CRTS) have become available. They can extend the quasar light curves by almost 50%. Indeed, Li et al. (2018) combined SDSS and Dark Energy Camera Legacy Survey (DECaLS) data, to provide a 15 year baseline, but by using an entire SDSS footprint suffered from poor sampling and had to use ensemble structure function approach.

Unlike previous studies, in this work, by combining SDSS and PS1 data we afford both an extended baseline (15 years), a large number (9000) of quasars, and a good cadence ($N > 60$ epochs) to which we fit the DRW model. The layout of this paper is as follows: first we confirm in Section 2 that extending the quasar baseline is the most important improvement in providing unbiased estimates of the DRW model parameters (K17); in Section 3 we describe the datasets employed, and their combination onto a common photometric system; in Section 4 we test the improvement in DRW parameters with simulation; finally in Section 5 we describe the main results analyzing correlations between physical parameters and variability, and in Section 7 we summarize the main results. In this work we adopt a Λ CDM cosmology with $h_0 = 0.7$ and $\Omega_m = 0.3$.

2. METHODS

2.1. DRW as a Gaussian Process

Damped Random Walk (Ornstein-Uhlenbeck process, Rasmussen & Williams 2006) can be modeled as a member of a class of Gaussian Processes (GP). Each GP is described by a mean and a kernel - a covariance function that contains a measure of correlation between two points: x_n and x_m , separated by Δt_{nm} (autocorrelation). For the DRW process, the covariance between two observations spaced by Δt_{nm} is:

$$\begin{aligned} k(\Delta t_{nm}) &= \sigma^2 \exp(-\Delta t_{nm}/\tau) \\ &= \sigma^2 ACF(\Delta t_{nm}) \end{aligned}$$

Here σ^2 is an amplitude of correlation decay as a function of Δt_{nm} , while τ is the characteristic timescale over which correlation drops by $1/e$. For a DRW, the correlation function $k(\Delta t_{nm})$ is also related to the autocorrelation function ACF .

Not explicitly used in this paper, but of direct relevance to the DRW modeling, is the structure function (SF). SF can be found from the data as the root-mean-squared of magnitude differences Δm calculated as a

function of temporal separation Δt (we drop subscripts n, m for brevity). SF is directly related to a DRW kernel $k(\Delta t)$:

$$SF(\Delta t) = SF_\infty (1 - \exp(-|\Delta t|/\tau))^{1/2} \quad (2)$$

For quasars SF follows approximately a power law: $SF \propto \Delta t^\beta$, and it levels out for large time lags Δt to a constant value of SF_∞ , as points in the lightcurve with large time separation cease to be correlated. Note that $SF_\infty = \sqrt{2}\sigma$ in the above (also see MacLeod et al. (2012); Bauer et al. (2009); Graham et al. (2015) for an overview).

2.2. Fitting

The likelihood for the particular value of DRW parameters given the data is evaluated with *celerite* - a fast GP solver (Foreman-Mackey et al. 2017). The underlying matrix algebra is similar to that used by Rybicki & Press (1992); Kozłowski et al. (2010), M10. Also, as in previous work, we use a prior on DRW parameters that is uniform in log space: $1/(\sigma\tau)$. The main difference in our approach is that rather than adopting the Maximum A-Posteriori (MAP) as the ‘best-fit’ value for the DRW parameters (as in Kozłowski et al. 2010, K17, Kozłowski 2016, M10, MacLeod et al. 2011), we find the expectation value using the marginalized log posterior. This is advantageous because of a non-Gaussian shape of the log posterior - if it were described by a 2D Gaussian, then the expectation value would coincide with the maximum of the log posterior.

2.3. The impact of light curve baseline

K17 reports that one cannot trust any results of DRW fitting unless the light curve length is at least ten times longer than the characteristic timescale. We confirm that the fidelity of DRW parameter retrieval does depend on the ratio of timescale to baseline, but we find that the baseline does not have to be ten times longer to provide meaningful, rather than unconstrained, results. To revisit relations between recovered and input timescale as a function of light curve baseline, we follow K17 in setting up a simulation of 10 000 DRW light curves with fixed length (baseline) $\Delta T = 8$ years, asymptotic variability amplitude of $SF_\infty = 0.2$ mag, SDSS or OGLE-like cadence, sampling over a range of input timescales. With fixed baseline, this spans the parameter space of $\rho = \tau/\Delta T$, $\rho \in \{0.01 : 15\}$. We simulate 100 light curves at each ρ .

The true underlying DRW signal $s(t)$ is found by iterating over the array of time steps t . At each step, we draw a point from a Gaussian distribution, for which the mean and standard deviation are re-calculated at each

timestep (see eqs. A4 and A5 in Kelly et al. 2009, as well as Sec. 2.2 in MacLeod et al. 2010). Starting at t_0 , the signal is equal to the mean magnitude, $s_0 = \langle m \rangle$. After a timestep $\Delta t_i = t_{i+1} - t_i$, the signal s_{i+1} is drawn from $\mathcal{N}(loc, stdev)$, with :

$$loc = s_i e^{-r} + \langle m \rangle (1 - e^{-r}) \quad (3)$$

and

$$stdev^2 = 0.5 SF_\infty^2 (1 - e^{-2r}) \quad (4)$$

where $r = \Delta t_i/\tau$, and τ is the damping timescale.

To simulate observational conditions we add to $s(t)$ - the true underlying signal, $n(t)$ - a noise offset :

$$y(t) = s(t) + n(t) \quad (5)$$

Like K17, we assume $n(t)$ to be drawn from a Gaussian distribution with zero mean and width σ , that corresponds to the photometric uncertainty. Likewise, we adopt SDSS S82-like cadence with $N=60$ epochs, or OGLE-III like cadence with $N=445$ epochs, and magnitude-dependent σ :

$$\sigma_{\text{SDSS}}^2 = 0.013^2 + \exp(2(r_{\text{SDSS}} - 23.36)) \quad (6)$$

$$\sigma_{\text{OGLE}}^2 = 0.004^2 + \exp(1.63(I_{\text{OGLE}} - 22.55)) \quad (7)$$

with $r_{\text{SDSS}} = 17$ mag and $I_{\text{OGLE}} = 18$ mag.

Fig. 1 shows the recovered ρ_{out} as a function of input ρ_{in} . We confirm the findings of K17: for short light curves, the best-fit τ becomes $\sim 1/2$ of light curve length (the ‘unconstrained’ region, lower-left of each panel). However, as long as the light curve is several times longer than the timescale ($\rho \gtrsim 3$), we can recover the timescale without bias (the dashed line approaches the solid diagonal line on both panels). Therefore, by extending the baseline we can move from the biased region (bottom left) to the unbiased regime (top right). This is the basis for this study, in which we extend the baselines of quasar light curves from SDSS-only (10 years) to combined SDSS-PS1 (15 years).

3. DATA

We focus on the data pertaining to a 290 deg^2 region of southern sky known as Stripe 82 (S82), repeatedly observed by the Sloan Digital Sky Survey (SDSS) between 1998 and 2008. Originally aimed at supernova discovery, objects in this area were re-observed on average 60 times (see MacLeod et al. 2012, Sec. 2.2 for overview, and Annis et al. 2014 for details). Availability of well-calibrated (Ivezić et al. 2007), long-baseline light curves spurred variability research (see Sesar et al. 2007). The

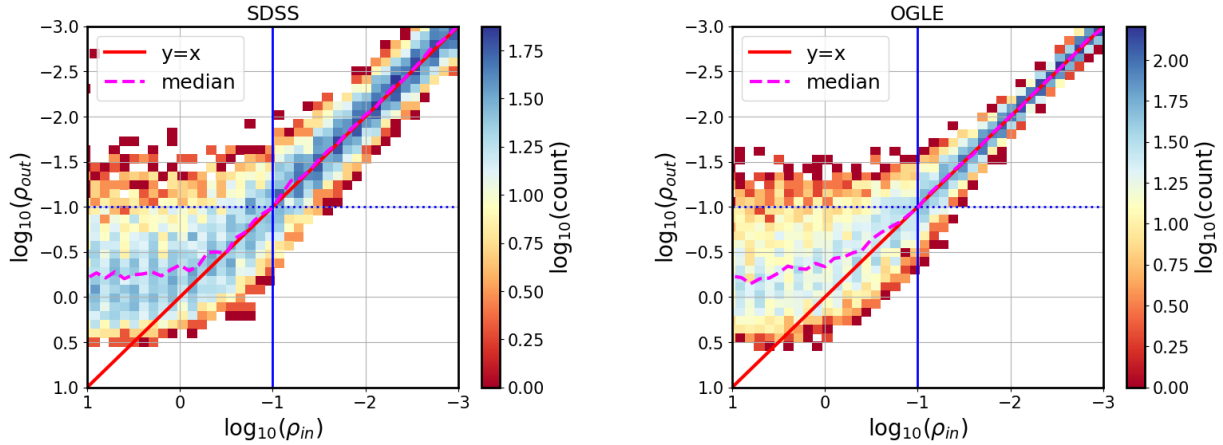


Figure 1. Probing the parameter space of $\rho = \tau/\Delta T$, with a simulation of 10 000 light curves : 100 light curves per each of 100 ρ values spaced uniformly in logarithmic space between $\rho \in \{0.01 : 15\}$. With a baseline ΔT set to 8 years, we sample a range of 100 input timescales. Left panel shows the SDSS-like cadence with $N=60$ epochs, and the right panel the OGLE-like cadence with $N=445$ epochs. The dotted horizontal and solid vertical lines represent $\rho = 0.1$, i.e. the baseline is ten times longer than considered timescale. The diagonal line is $y = x$, i.e. the line that would be followed if the recovered ρ (τ) was exactly the same as the input ρ (τ). Given a quasar light curve, which has one true underlying DRW timescale, as we extend the baseline, we move from the bottom-left (unconstrained) to the top-right (well-constrained) part of the parameter space.

catalog prepared by [Schneider et al. \(2008\)](#) as part of DR9 contains 9258 spectroscopically confirmed quasars. Within $0.5''$ we find matching data for 9248 quasars from PanSTARRS (PS1) DR2 ([Chambers 2011](#); [Flewelling 2018](#)), xxx from Catalina Real-Time Transient Survey (CRTS, [Drake et al. 2009](#)), and xxx from Palomar Transient Factory (PTF, [Rau et al. 2009](#)). Fig. 2 illustrates the improvement in baseline coverage when combining various surveys. The width of each rectangle corresponds to the duration of each survey (survey baseline), and the height to the area covered by each survey. The lower edge of each rectangle marks the 5σ depth in the r-band (or equivalent). LSST stands out as providing the best extension of SDSS baseline, and depth.

Combining data from different photometric standards would require applying color transformation, or photometric offsets. We first seek to combine PS1 gri, PTF gR, and CRTS V, into a common SDSS r-band (best photometry). To this end we calculate color terms using the SDSS standard stars catalog ([Ivezić et al. 2007](#)). Focusing on a 10% subset of randomly chosen standard stars, we find their CRTS, PS1, and PTF matches ¹.

The difference between the target (SDSS) and source (eg. PS1) photometry can be written as a function of the mean SDSS ($g-i$) color:

$$m_{\text{PS1}} - m_{\text{SDSS}} = f(g-i) \quad (8)$$

¹ CRTS from B.Sesar, priv.comm., PS1 from MAST <http://panstarrs.stsci.edu>, and PTF from IRSA PTF Object Catalog <https://irsa.ipac.caltech.edu/>

Some authors (eg. [Li et al. 2018](#)) allow the transformation to be a higher-order polynomial, but as Fig. 3 shows, quasars occupy a relatively narrow region of ($g-i$) color space, and we find that the linear fit is sufficient. We thus find the photometric offset between SDSS and PS1 gri, PTF gR, and CRTS V, as a function of SDSS $g-i$ color (see Table 1 for details). An example of SDSS-PS1 offsets is shown on Fig. 4. Note that the PS1 r-band is very close to the SDSS r-band (middle panel), within 0.01 mag (1% level) across the SDSS ($g-i$) color range. Fig. 5 illustrates that this is also true as a function of SDSS r magnitude, all the way to $r < 20.5$. Because of that, we also combine PS1 r-band and SDSS r-band without applying any offsets.

In selecting the most beneficial datasets to complement SDSS we also considered the error distribution. As shown on Fig. 2, PTF and CRTS are much shallower than SDSS or PS1. Therefore they would have larger photometric uncertainties for faint objects, like quasars (median 20 mag) - see Fig. 6. Simulations show that due to larger errors PTF and CRTS while extending the SDSS baseline also decrease the overall quality of the light curves by making them more noisy.

It turns out that, as we test with simulations in Sec. 4, the best improvement in recovery of quasar DRW parameters is obtained by utilizing only SDSS and PS1 data. This is partly due to both surveys having similar photometric depth (Fig. 2), and therefore comparable distributions of photometric uncertainties (Fig. 6). Furthermore, to mitigate the problems that could arise when applying photometric transformations of PS1 g,i

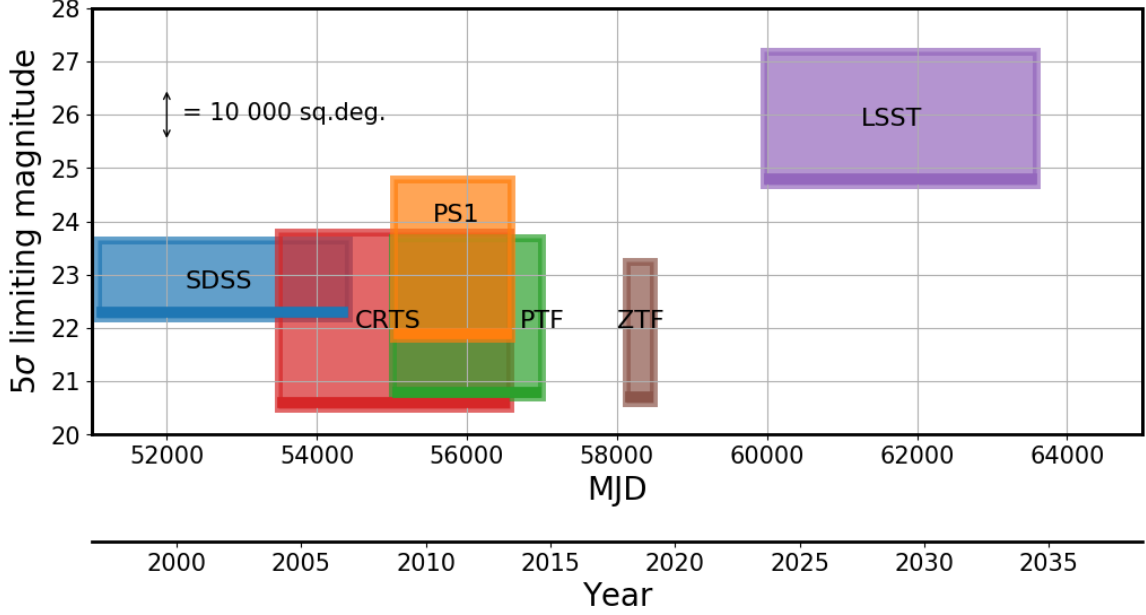


Figure 2. An illustration of survey baseline, sky area covered, and depth. The width of each rectangle corresponds to the extent of light curves available (or simulated) for Stripe 82 quasars for each survey. For SDSS this means DR7; for CRTS DR2, PS1 DR2, PTF DR2, ZTF year 2018, and LSST the full 10-year survey. The lower edge of each rectangle (marked by a solid thick line) corresponds to the 5σ limiting magnitude (SDSS r, PS1 r, PTF r, ZTF r, LSST r, CRTS V). The vertical extent corresponds to the total survey area (for SDSS, up to and including DR15). Note how PS1 and PTF extend the baseline of SDSS by approximately 50%, and how inclusion of LSST triples the SDSS baseline. For reference, the area covered by LSST is 25000 sq.deg., which corresponds to 60% of the sky. The whole sky has an area of 4π steradians (41253 sq.deg.).

to SDSS r, we end up using only SDSS r and PS1 r, with no offsets applied.

Similarly to Charisi et al. (2016); Suberlak et al. (2017), we perform light curve cleaning. Of 8516 light curves with 662 092 epochs, we remove 14 156 5σ outliers in photometric uncertainty and magnitude space. We also perform day averaging (error weighted) when more than 1 epoch was available per night, which further reduces the number of epochs by 67 615. If combined nightly error was < 0.02 , we add in quadrature 0.01 mag. In the final sample there are 580 321 epochs.

4. SIMULATIONS : LESSONS LEARNED

We simulate the theoretical improvement of the DRW parameter retrieval in extended light curves. We generate long and well-sampled ‘master’ light curves, all with input $\tau = 575$ days, $SF_\infty = 0.2$ mag (the median of S82 quasar distribution in M10), with a mean of 0. We then subsample at real observed epochs for SDSS and PS1, and at predicted cadences for ZTF and LSST (see Fig. 7). To each such simulated light curve we add a magnitude offset corresponding to the mean of each SDSS-PS1 segment. That way the magnitude distribution of simulated light curves is similar to that of the observed SDSS-PS1 data. For the LSST 10-year segment (finishing in 2031) we assumed 50 epochs per

Table 1. Color terms (offsets) between CRTS, PTF, PS1 passbands used in combined light curves, and SDSS, using the mean $(g - i)_{\text{SDSS}}$ color to spread the stellar locus. Thus the r_{SDSS} synthetic magnitude (r_s for short) can be found as $r_s = x - B_0 - B_1(g - i)_{\text{SDSS}}$. This linear trend is illustrated on Fig. 4, where we plot $(x - r_{\text{SDSS}})$ as a function of $(g - i)_{\text{SDSS}}$ for $x = g_{\text{P1}}, r_{\text{P1}}, i_{\text{P1}}$.

Band (x)	B_0	B_1
CRTS V	-0.0464	-0.0128
PTF g	-0.0294	0.6404
PTF R	0.0058	-0.1019
PS1 g	0.0194	0.6207
PS1 r	0.0057	-0.0014
PS1 i	0.0247	-0.2765

NOTE—To derive the color terms we used SDSS S82 standard stars catalog (Ivezić et al. 2007). We randomly selected 10% of that catalog, for which 48250 have CRTS light curves. We obtained PS1 photometry from MAST, and PTF from IRSA PTF Object Catalog. We imposed quality cuts requiring that the stars are bright: $r < 19$.

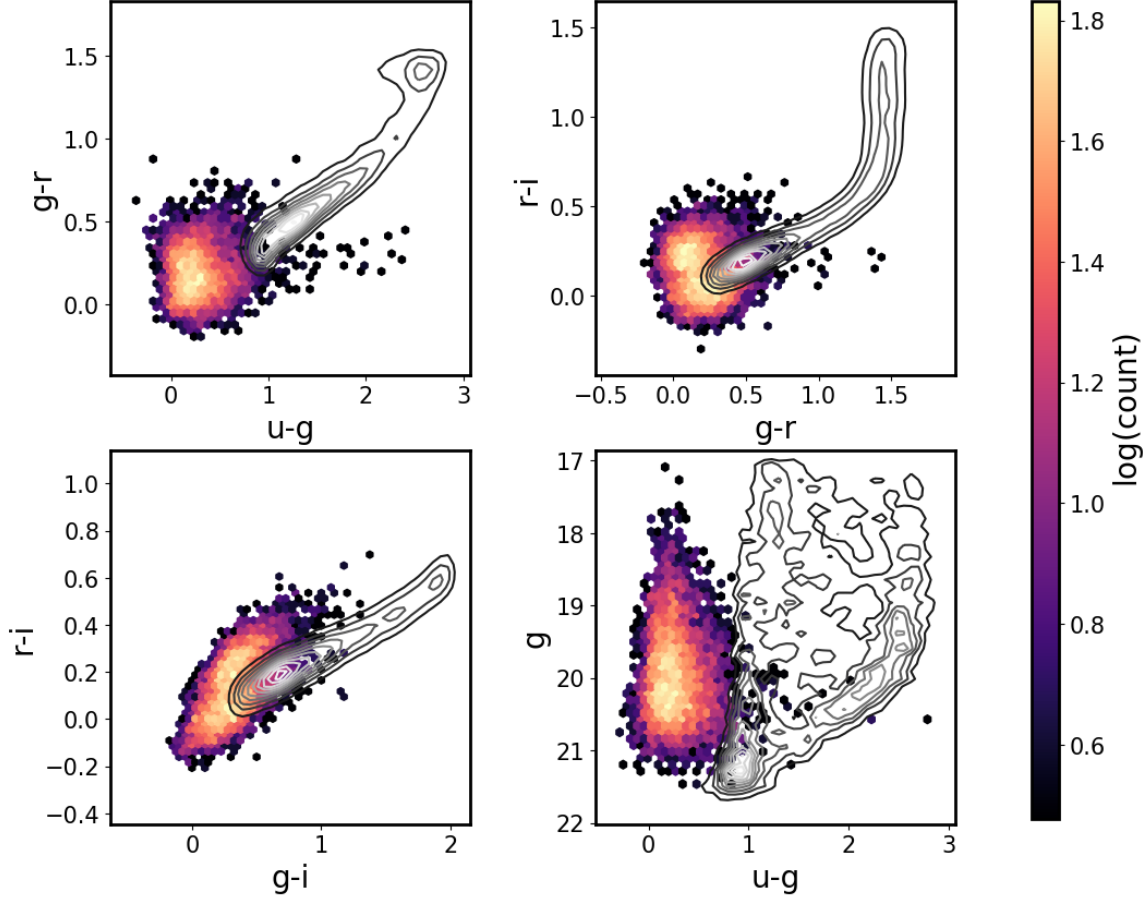


Figure 3. Regions of color-color (upper left, upper right, bottom left), and color-magnitude (bottom right) space occupied by SDSS S82 quasars (color) and stars (contours). We use quasar median photometry from [Schneider et al. \(2010\)](#), and standard stars catalog of [Ivezić et al. \(2007\)](#), showing a random subset of 10 000 stars. We find the SDSS-PS1 color terms using the region of SDSS color space that best represents quasars, that are generally bluer than the stellar locus: $-0.5 < (g - i) < 1$. Quasars also overlap other variable sources (eg. RR Lyrae), not shown here ([Sesar et al. 2007](#)).

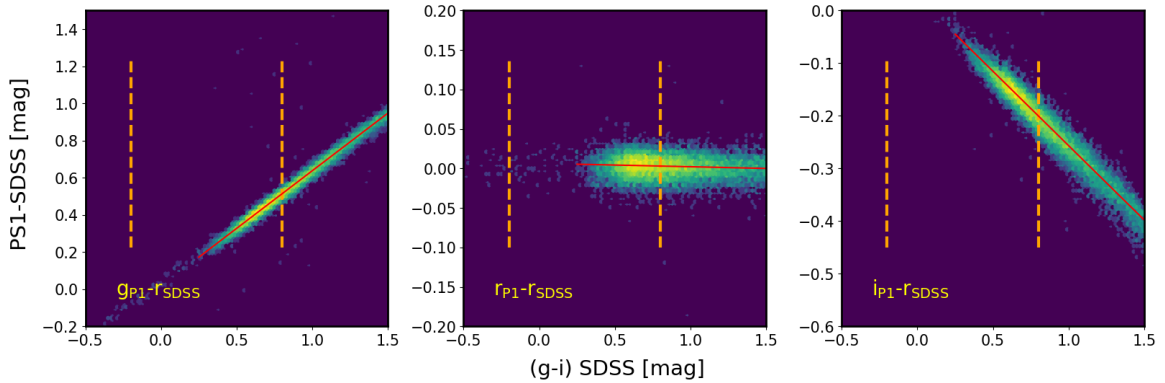


Figure 4. The SDSS-PS1 offsets, derived from the SDSS standard stars catalog ([Ivezić et al. 2007](#)). From randomly chosen subset of 50 000 stars, we selected only 23 000 that are sufficiently bright ($r_{\text{SDSS}} < 19$) to minimize scatter due to photometric uncertainty. On each panel we plot 20 000 SDSS stars that have PS1 match within 0.1 arcsec. Vertical dashed lines mark the region in the SDSS color space occupied by quasars (see Fig. 3), used to fit the stellar locus with a first order polynomial, marked by the solid red line.

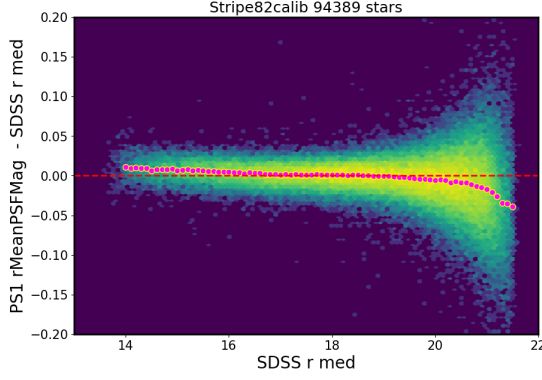


Figure 5. Of 100 000 randomly selected stars from 1 mln SDSS standard stars catalog almost 95 000 have PS1 DR2 photometry. For these we plot the difference in PS1 r-band and SDSS r-band as a function of SDSS magnitude. We overplot the median offset as filled magenta circles. There is a very slight slope, but all the way up to $r < 20.5$ the median difference is less than 0.01 mag (1 % level).

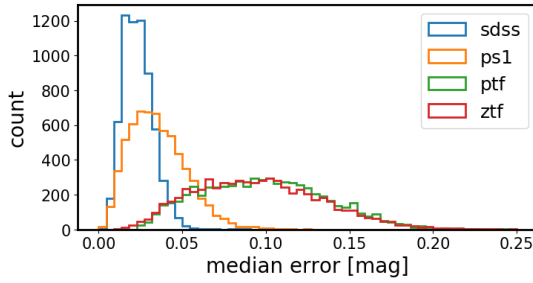


Figure 6. Distribution of median photometric uncertainties (‘errors’) in combined r-band real light curves. This shows that the PTF and ZTF segments have much larger errors than SDSS, PS1 due to shallower depth data. This is the reason for using only SDSS-PS1 part of the combined light curve.

year, randomly distributed throughout the year, with the following error model:

$$\begin{aligned} \sigma_{LSST}(m)^2 &= \sigma_{sys}^2 + \sigma_{rand}^2 \text{ (mag)}^2 \\ \sigma_{rand}^2 &= (0.04 - \gamma)x + \gamma x^2 \\ x &= 10^{0.4(m-m_5)} \end{aligned} \quad (9)$$

with $\sigma_{sys} = 0.005$, $\gamma = 0.039$, $m_5 = 24.7$ (see Ivezić et al. 2019, Sec.3.2). For the ZTF 1-year segment (Spring 2019 ZTF DR1 including the data from 2018) we assumed 120 observations (every three nights) in g_{ZTF} and r_{ZTF} , deriving the magnitude-dependent error model by plotting for ZTF standard stars in Fig. 8 best mag rms as a function of best median magnitude. We find that the LSST error model (Eq. 9) with $\gamma = 0.05$, $\sigma_{sys} = 0.005$, and $m_5 = 20.8$ adequately describes the ZTF photometric uncertainty.

To mirror observational conditions we add to the true underlying DRW signal a Gaussian noise, with variance defined by photometric uncertainties for corresponding surveys. Given the noise properties of each survey (Fig. 6), we find that relatively large uncertainties of CRTS and PTF segments introduce less improvement in recovery of DRW parameters, with a similar baseline already afforded by the PS1 data (Fig. 2). We also checked that inclusion of ZTF data for 2018 would not significantly change our results. Using PS1 data with its excellent deep photometry (as compared to ZTF or PTF) is the best improvement over existing SDSS results. In the future (after more data has been assembled and re-calibrated) ZTF will help, but not as dramatically as LSST (see Figs. 9 and 22). For this reason we use only SDSS-PS1 portion of quasar light curves, as the best tradeoff between adding more baseline vs introducing more uncertainty with noisy data.

5. RESULTS: VARIABILITY PARAMETERS FOR S82 QUASARS

We extend Stripe82 quasar light curves by combining the SDSS r-band data with the r_{PS1} data, without any photometric offsets. For each quasar we fit the SDSS and SDSS-PS1 segments with the DRW model. This yields two sets of DRW parameters per quasar: $(\tau_{SDSS}, SF_{\infty, SDSS})$, and $(\tau_{SDSS-PS1}, SF_{\infty, SDSS-PS1})$. Because variability is inherent to the quasar, for the remaining analysis we shift all fitted timescales to quasar rest frame, and implicitly assume that the DRW timescales are considered in rest frame: $\tau_{RF} = \tau_{OBS}/(1+z)$.

In this section we first correct fitted τ , SF_{∞} for wavelength dependence. Then we show the consistency with M10 results, and consider the trends between DRW parameters and physical quasar properties: black hole mass M_{BH} , absolute i-band magnitude M_i , or redshift z .

5.1. Comparison to M10

The DRW parameters recovered with *celerite* are broadly consistent with M10 - Fig. 10 shows the rest-frame τ , and SF_{∞} distributions for our results for the SDSS segment (blue dashed line), SDSS-PS1 combined light curves (green dot-dashed line), and M10 SDSS for r-band only (red solid line). When using the same data as M10 (SDSS), our results agree. A detailed object-by-object comparison on Fig. 11 reveals a slight offset between log-ratios of DRW parameters, which can be attributed to software differences.

5.2. Rest-frame Wavelength Correction

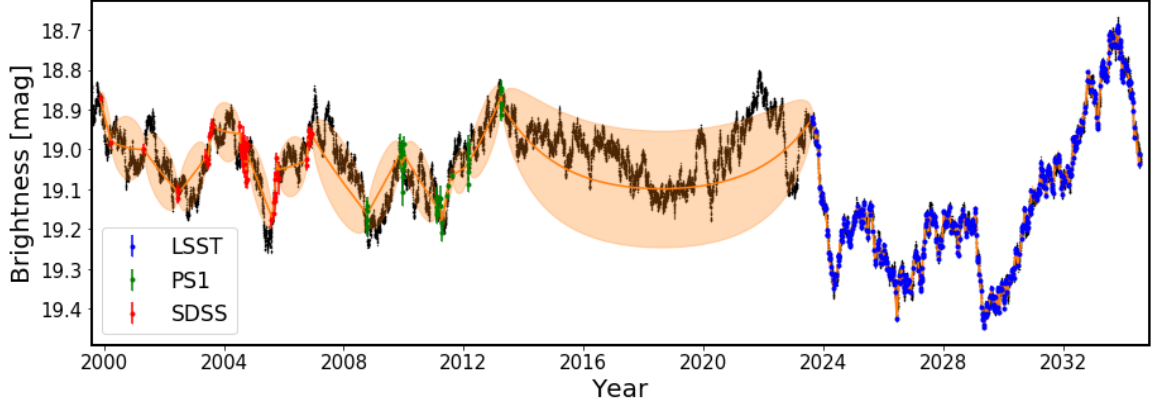


Figure 7. Simulated well-sampled underlying DRW process - one of ‘master’ light curves ($\tau = 575\text{d}$, $SF_\infty = 0.2\text{ mag}$, 4 points per day) shown with small black dots. To simulate observations, the cadence is degraded (subsampling) to match the ground-based cadence corresponding to real quasar data from SDSS (red), PS1 (green) segments, and simulated LSST (blue) epochs (here we use SDSS-PS1 epochs for quasar dbID=3537034). The orange ‘error snake’ is an envelope marking the standard deviation of the fit to the data using a Gaussian process with DRW kernel (Sec. 4).

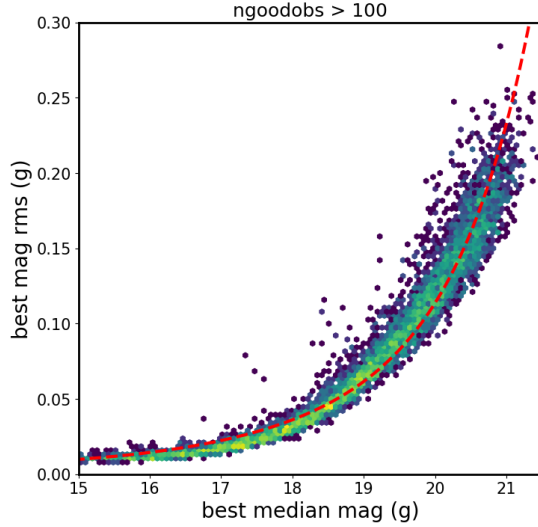


Figure 8. The best mag rms plotted as a function of magnitude for ZTF non-variable stars with over 100 observations. We overplot the adopted error model, with $\gamma = 0.05$, $\sigma_{\text{sys}} = 0.005$, and $m_5 = 20.8$ (see Eq. 9). Properties of ZTF photometric uncertainties are largely similar to the PTF uncertainties.

Since quasars are located at non-negligible redshifts, the observed wavelengths (eg. through the SDSS bandpass), depending on the redshift, probe a region of shorter wavelengths in emitted spectrum: $\lambda_{\text{obs}} = \lambda_{\text{RF}}(1+z)$ (see Shen et al. 2018, Fig.7). Thus to compare variability of the same parts of the rest-frame spectrum, we need to estimate the rest-frame emission wavelength λ_{RF} , and correct for the dependence of variability parameters (τ, SF_∞) on λ_{RF} . Since this study only used r-band light curves, on Fig. 15 we illustrate the wavelength dependence of τ, SF_∞ with M10 SDSS *urz* data.

We overplot with red contours the new fit results using only the SDSS portion of each light curve, and with orange contours the fit results using combined SDSS-PS1 light curves. We take the center of each bandpass to approximate the observed wavelength. That is for SDSS *urz* bandpasses, $\lambda_{\text{obs}} = 3520, 6250, 9110\text{ \AA}$, respectively. Then for each quasar the rest-frame wavelength (corresponding to the bandpass center) is estimated given its redshift: $\lambda_{\text{RF}} = \lambda_{\text{obs}}/(1+z)$. On top of τ, SF_∞ as a function of λ_{RF} scaled to 4000 \AA , we plot a power law dependence employed by M10:

$$f \propto \left(\frac{\lambda_{\text{RF}}}{4000\text{ \AA}} \right)^B \quad (10)$$

with $B = -0.479$ and 0.17 for SF_∞ and τ , respectively. We use this relationship to shift the rest-frame SF_∞ and τ to 4000 \AA .

5.3. Trends with Black Hole Mass, Absolute Luminosity

Correlations between variability parameters and the physical properties of quasars are of high utility. In the era of large synoptic surveys (ZTF, LSST), only a few percent of AGN with optical time-series will be followed up with spectroscopy (Ivezić et al. 2019). A relationship where $(\tau, SF_\infty) = f(M_i, M_{\text{BH}})$ would allow to infer black hole masses and luminosities for millions of quasars.

Since S82 quasars are spectroscopically-confirmed, we use estimates of quasar physical properties, such as black hole mass, or absolute luminosity M_i , from Shen et al. (2011), based on single-epoch spectra. M_i in that catalog is K-corrected to the redshift of 2, $M_i(z=2)$, which corresponds the peak of quasar activity and requires the

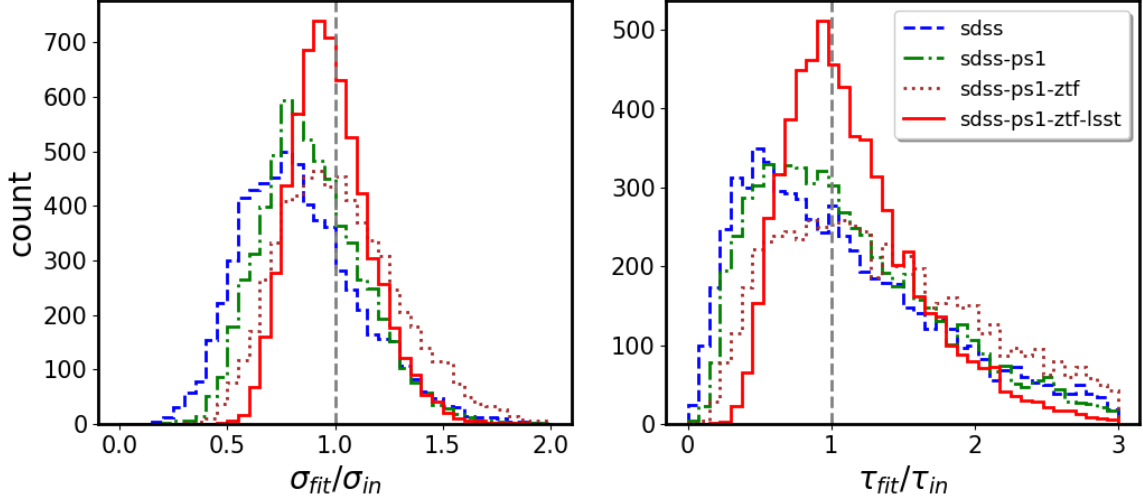


Figure 9. The ratio of DRW parameters fitted with *celerite*: τ and σ , to the input $\tau_{in} = 575\text{d}$, $\sigma_{in} = 0.2/\sqrt{2} \sim 0.14$ ($SF_{\infty} = 0.2$ mag). We simulated 9258 ‘master’ light curves, and subsampled at real SDSS r-band or PS1 r-band cadence and photometric uncertainties, and simulated ZTF and LSST cadence. To simulate observing conditions, the underlying DRW signal was convolved with a Gaussian noise corresponding to epochal errors. From each light curve we start with SDSS segment only, and as we add more segments (PS1, ZTF, LSST), we refit for DRW model parameters with *celerite*. Thus each line corresponds to a different segment of simulated combined SDSS-PS1-ZTF-LSST light curves. As we extend the baseline the histograms shift to towards the vertical dashed line that marks the input values of τ, σ . The improvement with the simulated first year of ZTF data is not as large as with LSST, due to significant baseline increase compared to SDSS-PS1 (see Fig. 2).

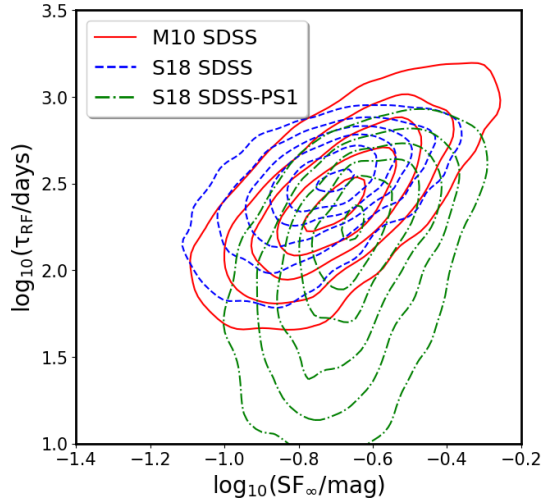


Figure 10. Comparison of distributions of the rest-frame variability timescale τ_{RF} against the asymptotic variability amplitude SF_{∞} , for M10 SDSS r-band, and *celerite* fits using SDSS or SDSS-PS1 segments of combined S82 quasar light curves. The M10 (red, solid lines) and this work, using only SDSS (dashed, blue), overlap, as we recover the same underlying distributions.

least extrapolation from the measured i-band (Richards et al. 2006). For details, see Appendix A.

To study the correlations between fitted DRW model parameters (τ, SF_{∞}) and quasar properties (M_i, M_{BH}), we first examine the intrinsic distribution of M_i, M_{BH} ,

as a function of redshift and observed i-band magnitude. Fig. 16 shows some trends, for instance the upward gradient in the top two panels reflects the selection effect that higher redshift quasars have to be brighter to be included in the magnitude-limited sample (luminosity-redshift degeneracy: see Sec.5, Fig.12 in M10, and Dong et al. 2018). Higher redshift quasars are also more active and have higher black hole masses due to cosmological downsizing (see Babić et al. 2007; Labita et al. 2009; McLure & Dunlop 2004). The distribution in the lower-left panel of Fig. 16 is peaked at $z = 2$ ($\log_{10}(1 + z) = 0.47$) which corresponds to the peak of quasar activity.

Now we consider the DRW parameters, τ and SF_{∞} (corrected for wavelength dependence), and their relation to quasar physical properties. Fig. 17 shows τ and SF_{∞} plotted as a function of M_{BH}, M_i , and z . The two left-hand side panels depict strong gradients of variability amplitude with M_i, z : brighter quasars have lower variability amplitude, largely independent of black hole mass.

To investigate these relations in more detail, we fit f (τ or SF_{∞}) as a power-law function of M_{BH}, M_i, z :

$$\log_{10} f = A + B \log_{10} (\lambda_{RF}/4000\text{\AA}) + C(M_i + 23) + D \log_{10} (M_{BH}/10^9 M_{\odot}) \quad (11)$$

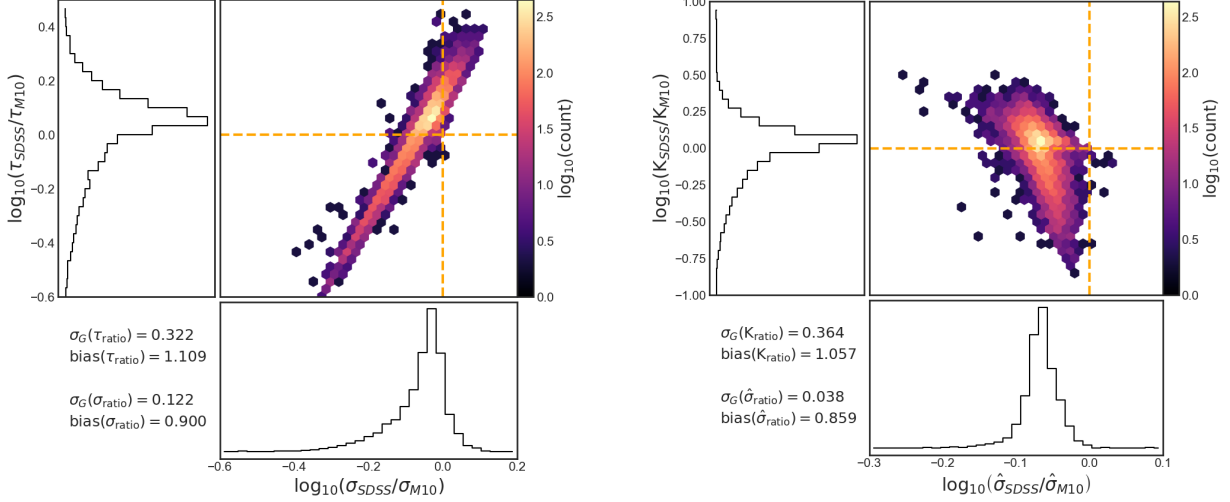


Figure 11. Comparison of *celerite* fits using only the SDSS r-band segments of S82 quasars ($\sigma_{\text{SDSS}}, \tau_{\text{SDSS}}$), against M10 results for SDSS r-band ($\sigma_{\text{M10}}, \tau_{\text{M10}}$), object-by-object. The small offset (< 0.05 dex) can be attributed to software differences. See Fig. 10 for a comparison of rest-frame τ and SF_{∞} distributions. This is similar to Fig.3 in M10, except we plot only the r-band SDSS results. The right-hand panel shows the comparison in an orthogonal $K - \hat{\sigma}$ space.

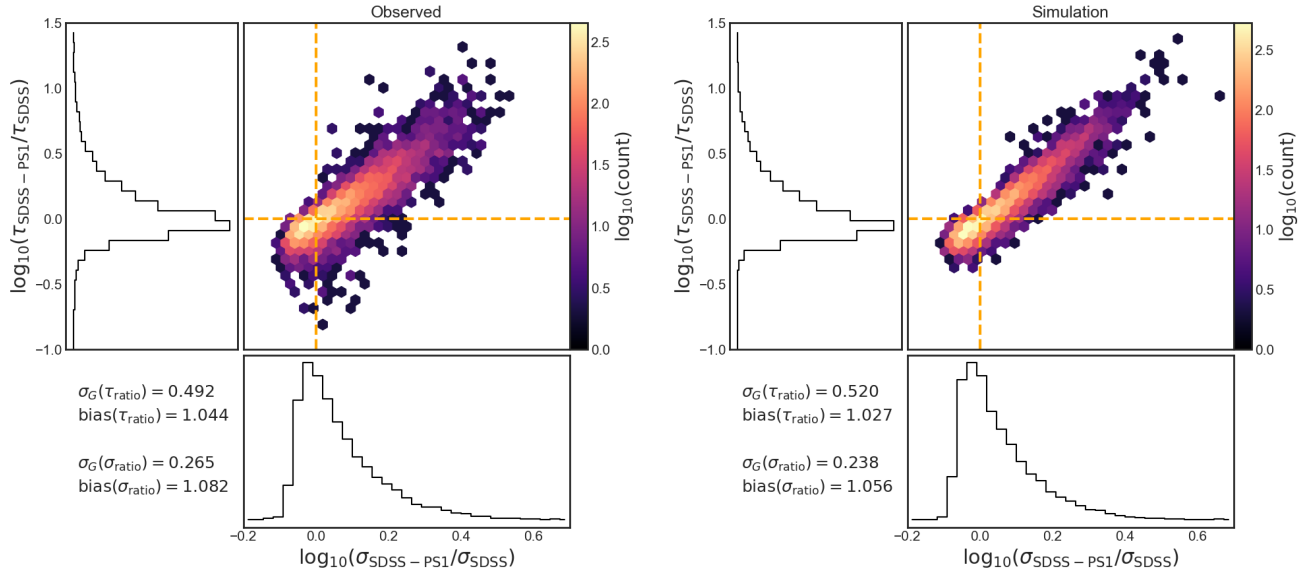


Figure 12. Ratios of fitted DRW parameters (τ, σ), comparing the value of parameter recovered using the combined light curve length (SDSS-PS1) to the shorter, SDSS-only light curve. The left panel shows the results for S82 quasars using real data, whereas the right panel shows the simulated quasars with realistic cadence, with $\tau_{\text{in}} = 575$ days and $SF_{\infty} = 0.2$ (right). The general trend when using the real data (despite having a range of underlying timescales and amplitudes) is similar to that when using simulated data: the diagonal scatter is along the lines of constant $\hat{\sigma}$, and there is much less scatter in the perpendicular direction of K (see Fig. 13. There is no major change of shape of distribution as a function of mean quasar magnitude.)

using a Bayesian linear regression method (Kelly 2007) that incorporates measurement uncertainties in all latent variables.

We compare the change in retrieved fit coefficients caused by adding PS1 data to SDSS against M10 SDSS-only study. Note that M10 fitted DRW model treating each of the 5 SDSS bands as a separate light curve, re-

sulting in over thirty thousand values of τ, SF_{∞} for nine thousand S82 quasars. Grouping fitted quasar parameters by band, they were correlated to quasar physical parameters with Eq. 11. Fig. 18 shows the posterior samples for fitting Eq. 11 to $f = SF_{\infty}$ for SDSS ugriz bands separately. It illustrates that each band yields a slightly different fit coefficient. M10 reported as the

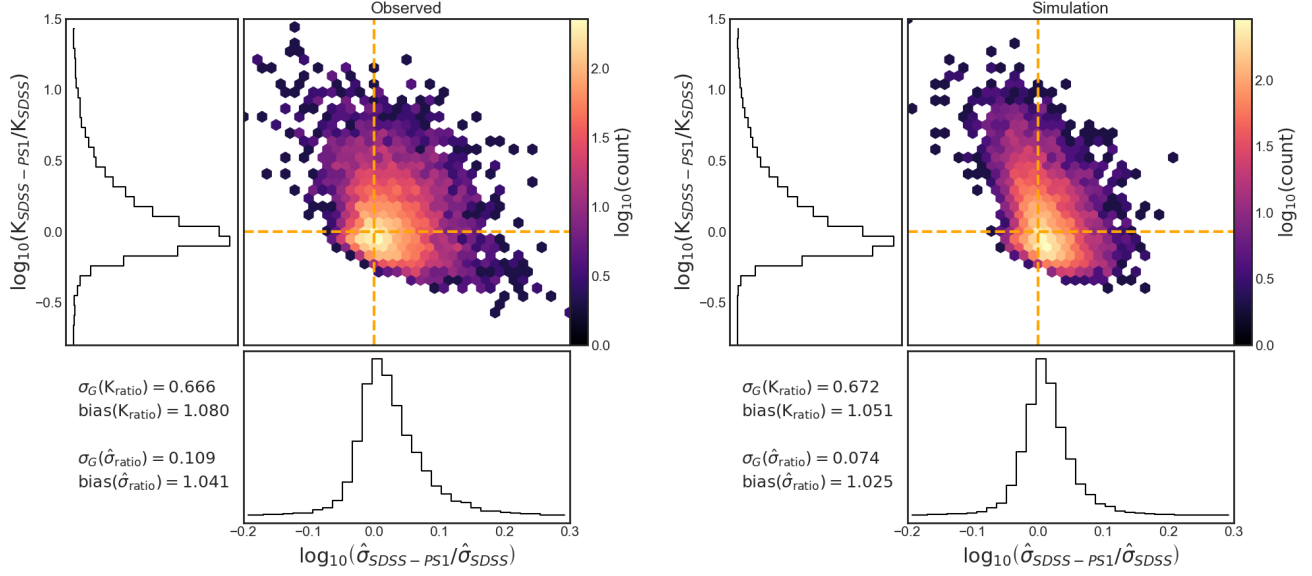


Figure 13. As Fig. 12, but in $K - \hat{\sigma}$ space, which is orthogonal to the $\tau - \sigma$ space, since $K = \tau\sqrt{SF_\infty} = \tau\sqrt{\sigma}2^{1/4}$ and $\hat{\sigma} = SF_\infty/\sqrt{\tau} = \sigma\sqrt{2}/\tau$.

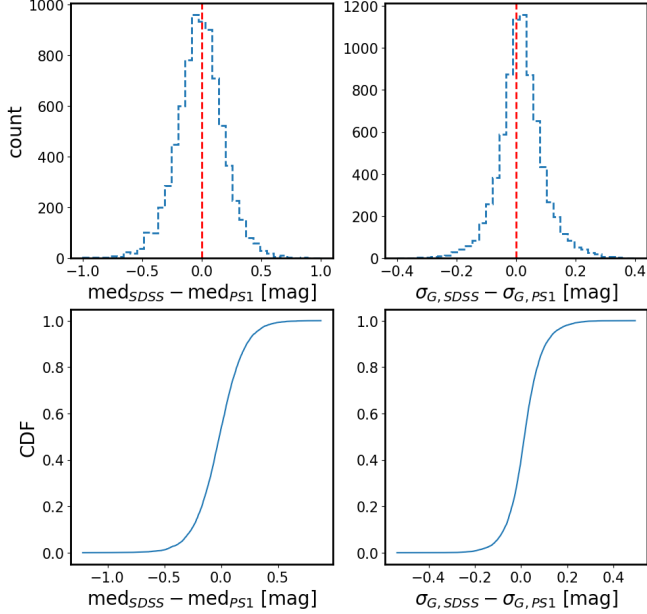


Figure 14. The differences between SDSS and PS1 segments of combined quasar r-band light curves. First, the difference between median SDSS and median PS1 portion, plotted as a histogram (upper-left panel), and cumulative distribution function (lower-left panel). Then, the difference between σ_G calculated for each portion of the light curve (defined as the difference between 75th and 25th percentile : $\sigma_G = 0.7413(Q_{75} - Q_{25})$ it is a robust estimate of the standard deviation of the underlying distribution). The outliers in the median offset space are also outliers in the DRW parameter space (eg. $\log(\tau_{SDSS-PS1}/\tau_{SDSS}) > 1$ and $\log(\sigma_{SDSS-PS1}/\sigma_{SDSS}) > 0.4$) and $r > 20.5$ all 38 candidates have median(SDSS)-median(PS1) > 0.1

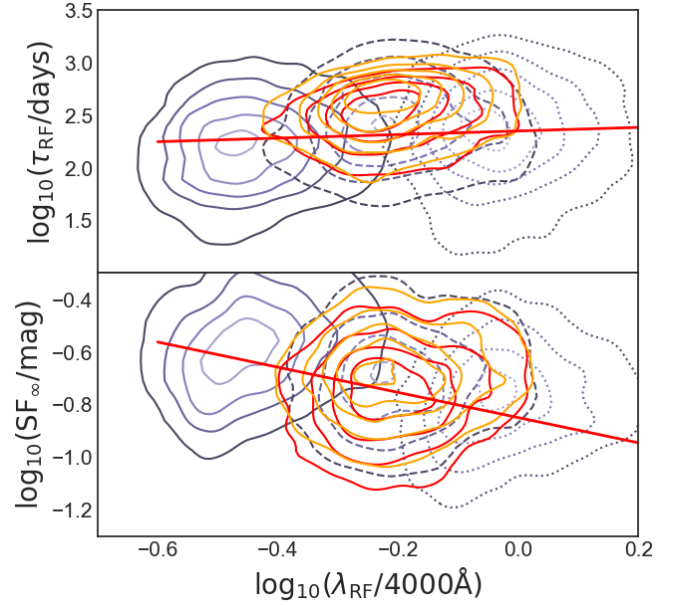


Figure 15. Rest-frame timescale τ (top panel), and asymptotic structure function SF_∞ (bottom panel), as a function of rest-frame wavelength λ_{RF} . The background contours show M10 SDSS urz data, and the foreground contours denote our results using SDSS (red) and SDSS-PS1 (orange) segments. The red line indicates the best-fit power law to M10 data, with $B = 0.17$ an -0.479 for τ_{RF} , and SF_∞ , respectively.

fit result the band-mean (red vertical dashed line), but since in this study we only use the combined r-band data, we compare our results directly to the mean of M10 SDSS r-band (green solid vertical line).

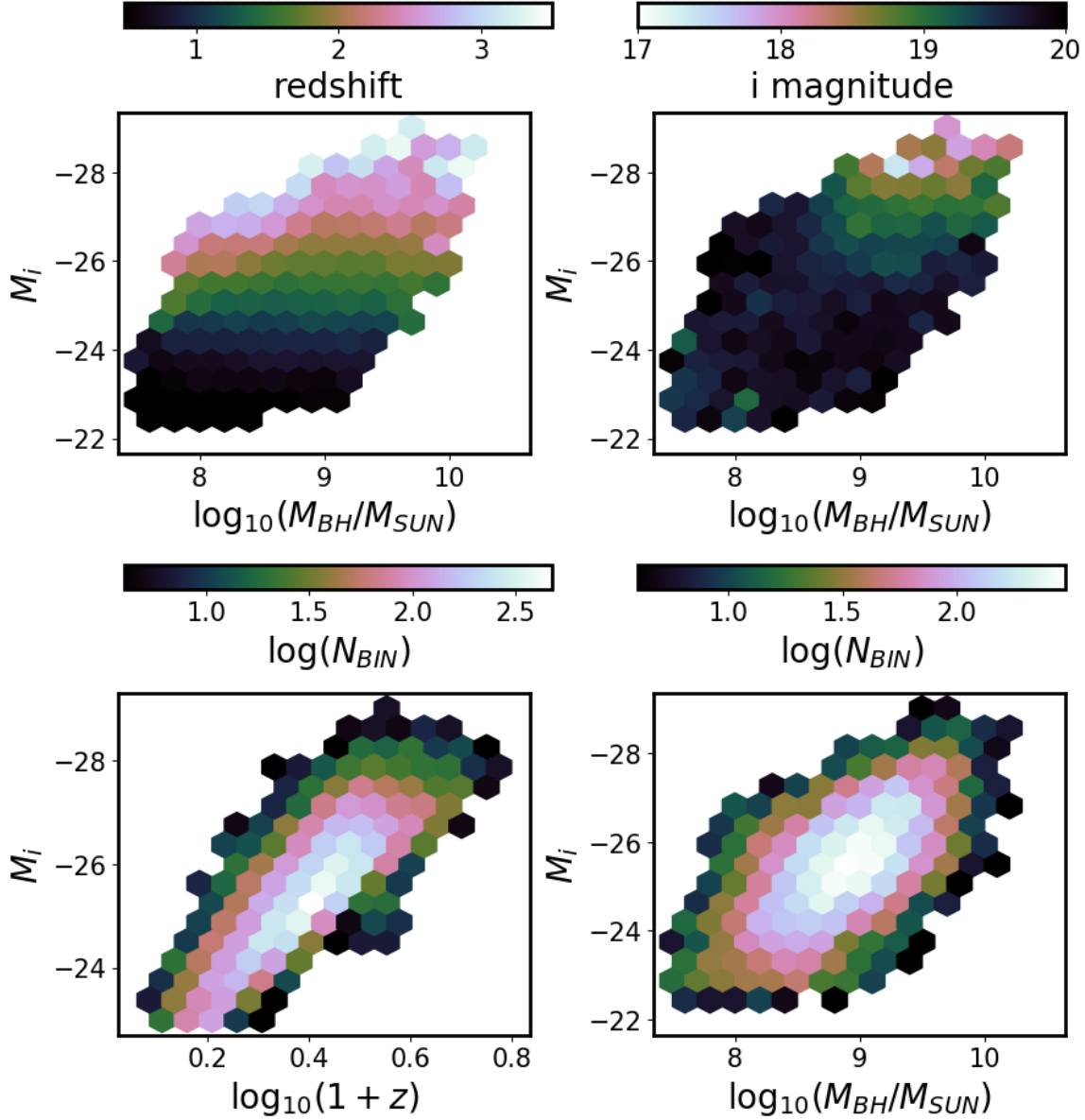


Figure 16. Distribution of quasars as a function of redshift, observed i-band magnitude, absolute i-band magnitude (K-corrected to $z=2$), and virial black hole mass. All taken from (Shen et al. 2011).

Subsequently we compare the results of fitting SDSS and SDSS-PS1 r-band data with *celerite*. Figs. 19 and 20 show the MCMC posterior draws from fitting Eq. 11 to M10, as well as our SDSS, SDSS-PS1 results (S19, this work). Mean and standard deviation of each distribution are summarized in Table 2. For $f=\tau$ above, Fig. 19 shows that the new data supports a stronger dependence of variability amplitude on quasar luminosity by 0.04 dex ($C \sim 0.06$ rather than ~ 0.02), but a weaker dependence on the black hole mass ($D \sim 0.09$ rather than ~ 0.16). For $f=SF_\infty$ above, Fig. 20 shows that there is a weaker trend with both luminosity ($C \sim 0.105$ rather

than ~ 0.117) and black hole mass ($D \sim 0.11$ rather than ~ 0.12), although the latter is a very small change.

5.4. Comparison to other studies: Eddington ratio

Dependence of both τ and SF_∞ on black hole mass and quasar luminosity can be understood as a function of accretion rate, encoded in the Eddington ratio: $f_{Edd} = L_{Bol}/L_{Edd}$, where $L_{Edd} = 1.26 \times 10^{38} (M_{BH}/M_\odot)$ erg/s (Shen et al. 2011). Fig. 21 shows the dependence of f_{Edd} and SF_∞ on M_i and M_{BH} . We find a much steeper power-law slope of -0.9 , against -0.23 reported in M10 from SDSS data.

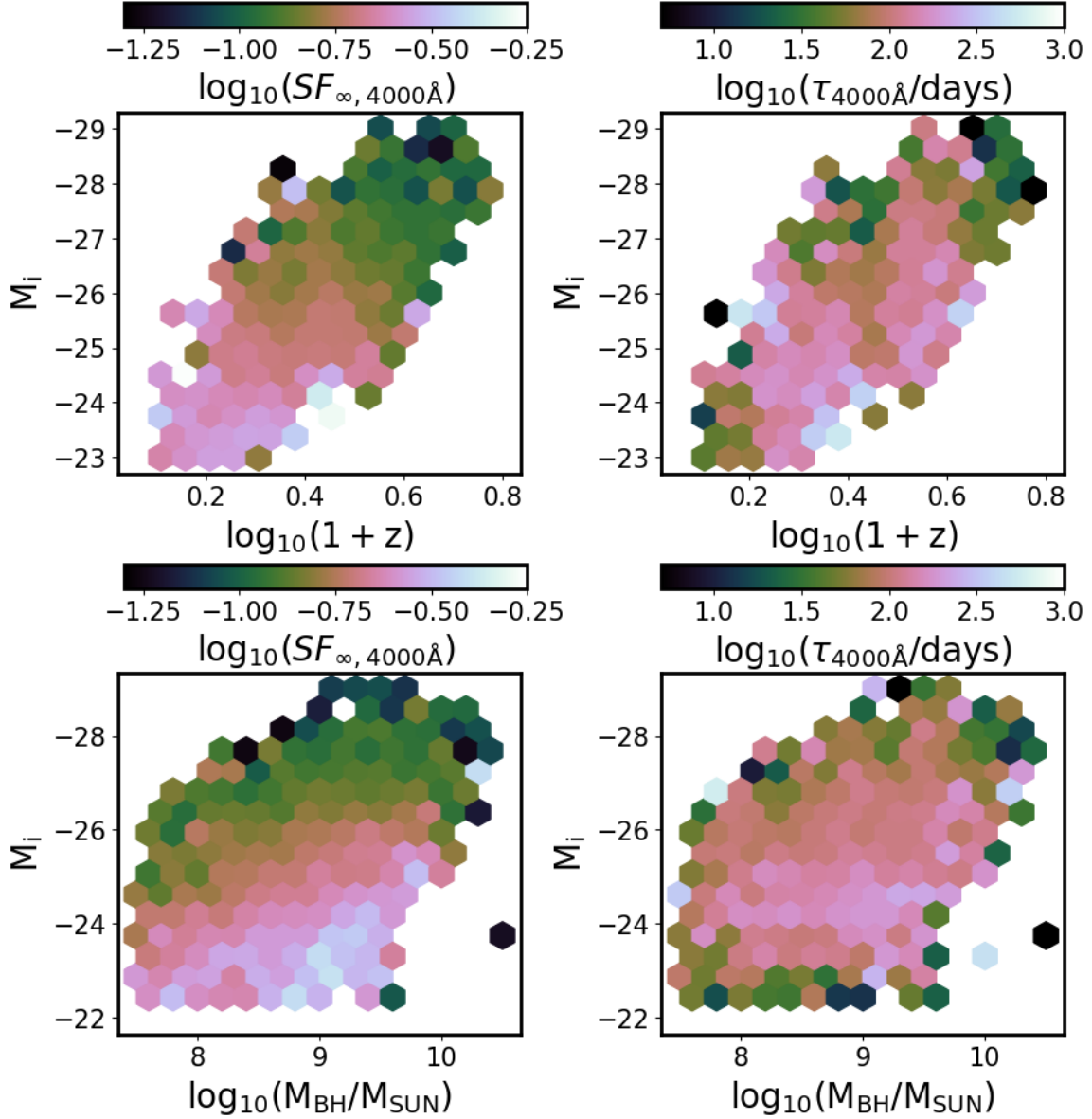


Figure 17. Long-term variability (SF_{∞}), and characteristic timescale (τ), as a function of absolute i-band magnitude (K-corrected to redshift 2, proxy for bolometric luminosity), virial black hole mass, and redshift.

Additional PS1 data extending SDSS quasar light curves suggests that characteristic variability timescale is more strongly dependent on luminosity. This is consistent with Sun et al. (2018), who concluded with Structure Function analysis of their luminosity-matched quasar sample, that τ depends mostly on the bolometric luminosity.

6. DISCUSSION

6.1. Trends with Eddington ratio

Anticorrelation of variability amplitude with the Eddington ratio has a variety of possible theoretical explanations. In the thin disk theory Shakura & Sunyaev

(1973); Frank et al. (2002); Netzer (2013), radius of the emission region at given wavelength increases with the Eddington ratio, and is inversely proportional to temperature (Rakshit & Stalin 2017). Thus a hotter disk means that the emission observed in a given bandpass is emitted from a larger radius. From causality, a smaller region can be more variable than a larger one. Therefore, a hotter disk would be less variable at a given wavelength than a colder one, and the variability amplitude as studied in a particular bandpass (here, SDSS r-band) would be anticorrelated with Eddington ratio (Fausnaugh et al. 2016; Edelson et al. 2015).

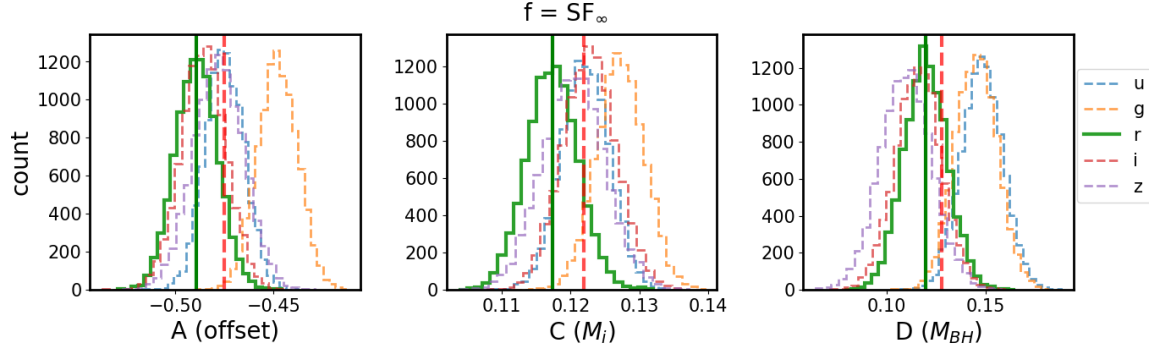


Figure 18. Wavelength dependence of DRW parameters (as fitted by M10), corrected for wavelength dependence, are correlated against M_i and M_{BH} (Shen et al. 2011). Results for each SDSS band are fitted separately for A, C, D coefficients in Eq. 11. The red dashed vertical line marks the mean of all band-averaged values, reported by M10 in Table 1. However, since we are fitting with r-band data only, we compare our results to the mean of M10 r-band results, marked with green solid vertical line.

Table 2. Comparison of best-fit coefficients for Eq. 11 using M10 results, and this work (S18). B is set to 0.17 or 0.479 from fitting a power law between λ_{RF} and τ , SF_∞ (see Fig. 15). For $f = \tau$, both C and D are almost the same between M10 and this work using SDSS only (rows 1 and 2). When using SDSS-PS1, C increases, and D is smaller than before (row 3). For $f = SF_\infty$, C and D are also the same between M10 and S19, SDSS (rows 4, 5), but when adding PS1 data, C and D become smaller (row 6).

f	Source	$A(\text{offset})$	$B(\lambda_{RF})$	$C(M_i)$	$D(M_{BH})$
τ	M10, SDSS	2.432 ± 0.026	0.17 ± 0.02	0.011 ± 0.009	0.163 ± 0.026
	S19, SDSS	2.603 ± 0.021	0.17 ± 0.02	0.022 ± 0.007	0.164 ± 0.021
	S19, SDSS-PS1	2.232 ± 0.029	0.17 ± 0.02	0.064 ± 0.01	0.094 ± 0.029
SF_∞	M10, SDSS	-0.489 ± 0.011	-0.479 ± 0.005	0.117 ± 0.004	0.12 ± 0.011
	S19, SDSS	-0.517 ± 0.01	-0.479 ± 0.005	0.117 ± 0.003	0.12 ± 0.01
	S19, SDSS-PS1	-0.467 ± 0.009	-0.479 ± 0.005	0.105 ± 0.003	0.111 ± 0.009

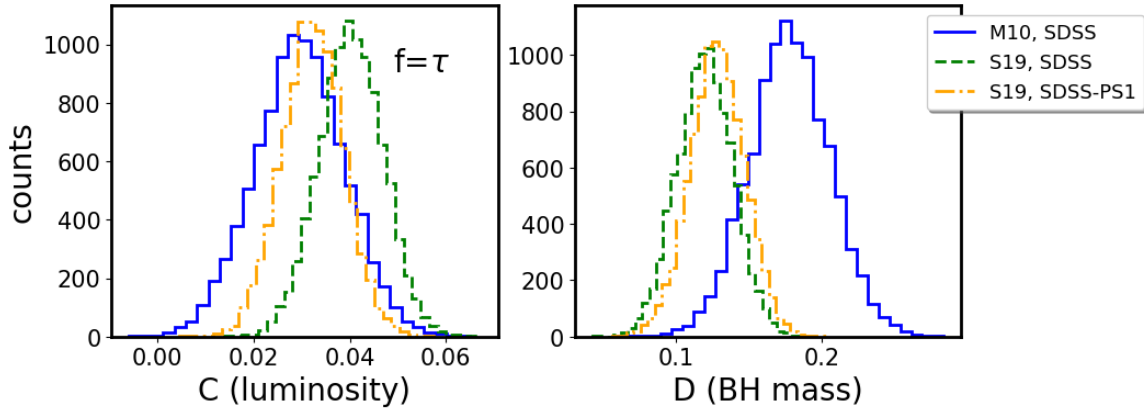


Figure 19. Distribution of posterior draws from MCMC Eq. 11, for $f = \tau$ with SDSS only (dashed green line), or SDSS-PS1 (dot-dashed yellow line) combined quasar light curves, against M10 SDSS r-band. Of 9258 quasars, the M10 selection criteria leave 6871 with trusted results. We find PS1 matches to 8516 quasars, and of these 6371 have matches to the subset of M10 quasars with trustworthy results in SDSS r-band. Each fit used the same subset of 6371 quasars, with either M10 SDSS-based results, S19 SDSS or SDSS-PS1 results. The results from both SDSS and SDSS-PS1 segments are consistent with M10 for the single band.

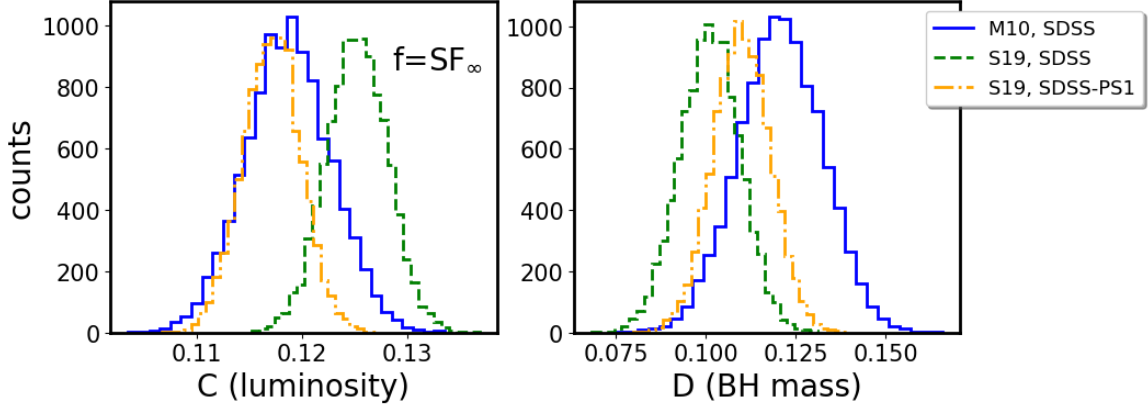


Figure 20. Same as Fig. 19, but fitting quasar absolute magnitude, and black hole mass in Eq. 11 as a function of the asymptotic amplitude $f = SF_\infty$. New data from PS1 is consistent with earlier results of M10.

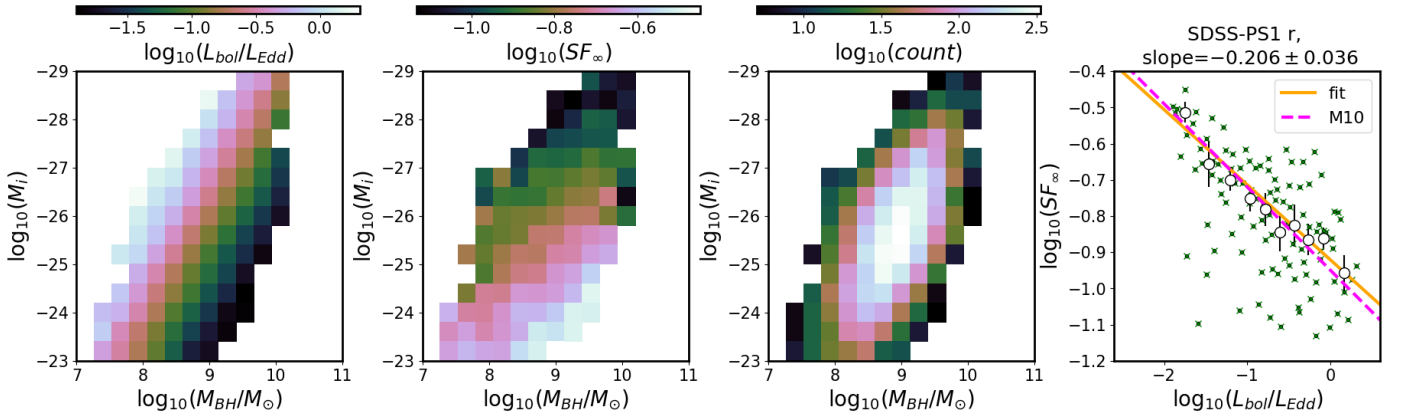


Figure 21. First panel: the Eddington ratio $f_{Edd} = L/L_{Edd}$ (from Shen et al. 2011) plotted as a function of M_{BH} vs M_i . Second panel: SF_∞ binned on the same grid of M_{BH} , M_i . Third panel: counts of quasars in each bin. We only plot bins with $N > 5$ quasars. Fourth panel: the median f_{Edd} and SF_∞ per bin are plotted as green crosses. These are aggregated along f_{Edd} , in 10 bins of such width that each has the same number of points. Open circles mark the median SF_∞ per f_{Edd} bin, with errors defined as $\sigma_y = 1.25\sigma_G(bin)/N$, where N is number of points per bin, and σ_G is the robust estimate of the standard deviation ($\sigma_G = 0.7413(Q_{75} - Q_{25})$). We assume the uncertainty along f_{Edd} as $\sigma_x = w/\sqrt{12}$, with w denoting the bin width. The solid orange line is the best-fit slope: -0.206 ± 0.036 assuming a first order polynomial, with the slope uncertainty estimated from the standard deviation of the posterior samples. This value is within error bars of M10 results (-0.23 ± 0.03).

On the other hand, in the strongly inhomogeneous disk model independent temperature fluctuations in N zones drive the variability (Dexter & Agol 2011). In that framework the inverse trend of variability amplitude against L/L_{Edd} and L_{Bol} can be understood qualitatively if more luminous quasars also have higher mass accretion rate, and thus greater number of disk inhomogeneities, resulting in smaller flux variability (Simm et al. 2016). The inhomogeneous disk model was consistent with mean SDSS spectral analysis in Ruan et al. (2014), but was not a preferred explanation for Kokubo (2015).

Both Rumbaugh et al. (2018) (with Dark Energy Survey structure function study) and Sun et al. (2018) (with a low- z subsample of S82 SDSS quasars) confirm the anti-correlation between quasar variability and luminosity. However, Graham et al. (2019) do not find support for this trend with the sample extremely variable quasars (EVQs) in the CRTS dataset, but when selecting for lower luminosity sources ($M_V < -23$), the anti-correlation is recovered. This is in accord with an interpretation that a dwindling fuel supply may correspond to higher variability. Furthermore, Sánchez-Sáez et al. (2018) combined the SDSS spectra with 5 year light curves of 2345 quasars obtained with Quasar Equatorial Survey Team (QUEST)-La Silla AGN Variability Survey, and using the Bayesian parametrization of Structure Function (Schmidt et al. 2010), $SF(\tau) = A(\tau/1\text{yr})^\gamma$, they also found that the amplitude of variability A is anti-correlated with rest-frame emission wavelength, and Eddington ratio (also see Simm et al. 2016, Rakshit & Stalin 2017).

Indeed, f_{Edd} is a proxy for the strength of accretion, which together with orientation may be the key to explaining quasar main sequence (QMS: (Shen & Ho 2014; Marziani et al. 2018)). The QMS, defined by so-called Eigenvector-1, is the the anti-correlation between the broad line FeII emission, and the strength of the narrow OIII (5007Å) line (Wang et al. 1996). An analysis of quasar clustering (Shen & Ho 2014), later confirmed by Sun & Shen (2015) with measurements of black hole mass from the quasar host galaxy stellar dispersion (Ferrarese & Merritt 2000; Kormendy & Ho 2013), showed that the entire diversity of quasars in QMS can be explained by the variation in accretion (affecting R_{FeII} - the ratio of the FeII EQ between 4435 – 4685 Å and H β), or orientation effects (affecting the FWHM of the H β). However, Panda et al. (2019a,b) found that these are insufficient, and variations in metallicity, as well as a range of cloud densities, and turbulences are required. Jiang et al. (2016) also found that metallicity, and in particular the iron opacity bump, may have a strong in-

fluence on the stability of an accretion disk, and thus linking metallicity to AGN variability. This is also consistent with findings of Sun et al. (2018): quasars with high FeII strength have higher metallicity, and have more stable disks.

6.2. Variability Timescales

In the era of changing-look active galaxies (including initially distinct classes of Changing-Look Quasars (LaMassa et al. 2015; MacLeod et al. 2019), Changing-Look AGNs (Marchese et al. 2012; Bianchi et al. 2009; Risaliti et al. 2009), Changing-Look LINERS (Frederick et al. 2019) to name a few) there is a revived interest in possibly linking the behavior of stellar-sized accreting systems (eg. Black Hole Binaries), to that of galactic scale (eg. AGN, QSO, LINERS)(Noda & Done 2018; Ruan et al. 2019).

It appears that there are several timescales at play, and possibly several interlinked mechanisms that drive the variability.

There is a hierarchy of relevant timescales in the standard optically thick, geometrically thin, α -disk model: dynamical, thermal, front, viscous, with $t_{dyn} < t_{th} < t_{front} < t_{visc}$ (Netzer 2013; Frank et al. 2002).

The dynamical, or gas orbital, timescale is simply an inverse of the Keplerian orbital angular frequency Ω at radius R :

$$t_{dyn} \sim 1/\Omega = \left(\frac{GM}{R^3} \right)^{-1/2} \quad (12)$$

The main parameter describing the accretion disk is α - the ratio of the (vertically averaged) total stress to thermal (vertically averaged) pressure (Lasota 2016):

$$\alpha = \frac{\langle \tau_{r\varphi} \rangle_z}{\langle P \rangle_z} \quad (13)$$

After Lasota (2016), the hydrodynamical stress tensor (corresponding to kinematic viscosity ν) is:

$$\tau_{r\varphi} = \rho \nu \frac{\partial v_\varphi}{\partial R} = \rho \nu \frac{d\Omega}{d \ln R} = \frac{3\rho \nu \Omega}{2} \quad (14)$$

so with c_s - local sound speed at radius R (isothermal sound speed is $c_s = \sqrt{P/\rho}$),

$$\alpha = \frac{3\rho \nu \Omega}{2P} = \frac{3\Omega \nu}{2c_s^2} \quad (15)$$

This means that smaller α corresponds to less viscous disks.

The thermal timescale, related to the time needed for re-adjustment to the thermal equilibrium (derived in detail in Frank et al. (2002)), is the ratio of heat content per unit disk area to dissipation rate per unit disk area:

$(dE/A)/(dE/dt/A) = dt$. The heat content per unit volume is $\sim \rho kT/\mu m_p \sim \rho c_s^2$, and heat content per unit area is $\sim \rho c_s^2/h \sim \Sigma c_s^2$. Meanwhile, the dissipation rate per unit area, $D(R)$, is

$$D(R) = \frac{9}{8} \nu \Sigma R^{-3} GM \quad (16)$$

(eq. 4.30 in Frank et al. 2002), so :

$$t_{th} \sim \frac{c_s^2 R^3}{GM \nu} = \frac{c_s^2}{\nu \Omega} = \frac{t_{dyn}}{\alpha} \quad (17)$$

Thus if the disk were inviscid ($\nu \rightarrow 0$), then $t_{th} \rightarrow \infty$ i.e. there is no contact with adjacent disk elements.

The cooling and heating fronts propagate through the disk at αc_s (Hameury et al. 2009) - in that description with no viscosity there is no communication between neighboring disk annuli, and thus no front propagation (Balbus & Hawley 1998; Balbus 2003). Following Stern et al. (2018), if we define as h/R the the disk aspect ratio, with the disk height $h = c_s/\Omega$, the characteristic time for front propagation is:

$$t_{front} \sim (h/R)^{-1} t_{th} \quad (18)$$

The viscous timescale is the characteristic time it would take for a parcel of material to undergo a radial transport due to the viscous torques from the radius R to the black hole (Czerny 2006). Note that while viscosity has probably magnetic origin (Eardley & Lightman 1975; Grzędziński et al. 2017), in this simplistic order of magnitude estimate we use a hydrodynamical description of accretion flow. With $\nu = \eta/\rho$ (kinematic viscosity being the ratio of dynamical viscosity to density), Frank et al. (2002) shows (Chap.5.2) that

$$t_{visc} \sim R^2/\nu \sim R/v_R = (h/R)^{-2} t_{th} \quad (19)$$

We can parametrize each timescale for a black hole mass $M_{BH} = 10^8 M_\odot$, at $R \sim 150 r_g$, with the gravitational radius $r_g = GM_{BH}/c^2 \sim 4 \text{ au}$, using Eqs.5-8 in Stern et al. (2018) :

$$t_{dyn} \sim 10 \text{ days} \left(\frac{M_{BH}}{10^8 M_\odot} \right) \left(\frac{R}{150 r_g} \right)^{3/2} \quad (20)$$

$$t_{th} \sim 1 \text{ year} \left(\frac{\alpha}{0.03} \right)^{-1} \left(\frac{M_{BH}}{10^8 M_\odot} \right) \left(\frac{R}{150 r_g} \right)^{3/2} \quad (21)$$

$$t_{front} \sim 20 \text{ years} \left(\frac{h/R}{0.05} \right)^{-1} \left(\frac{\alpha}{0.03} \right)^{-1} \left(\frac{M_{BH}}{10^8 M_\odot} \right) \left(\frac{R}{150 r_g} \right)^{3/2} \quad (22)$$

$$t_{visc} \sim 400 \text{ years} \left(\frac{h/R}{0.05} \right)^{-2} \left(\frac{\alpha}{0.03} \right)^{-1} \left(\frac{M_{BH}}{10^8 M_\odot} \right) \left(\frac{R}{150 r_g} \right)^{3/2} \quad (23)$$

In summary, of considered timescales only thermal and dynamical are short enough to be related to the observed short-term stochastic variability. It may be that the variability on the scale of days is driven by local changes, and on the longer scale (perhaps hundreds of days) by a different mechanism (Kokubo 2015). The other time scales may be more related to the dramatic changes in brightness of the continuum as observed in changing-look AGN - Noda & Done (2018) favor a change in mass accretion rate, followed by a propagation of the cooling front Lawrence (2018); Simm et al. (2016). Noda & Done (2018) also suggests that perhaps some short-term variability could be related to the amount of the disk swept by the thermal front propagation due to Hydrogen ionization instability, similarly to white dwarf systems (also, see Ruan et al. 2019; Ross et al. 2018; Śniegowska & Czerny 2019).

The variability on several years timescale could also be explained by the X-ray reprocessing model Kokubo (2015); Kubota & Done (2018), assuming that the AGN UV-optical variability is a results of reprocessing of X-ray or far-UV emission (Krolik et al. 1991). The idea of X-ray reprocessing over time has gained more and more support, with evidence from simultaneous X-ray-UV-optical AGN time series (Edelson et al. 2014; McHardy et al. 2018; Zhu et al. 2018). In particular, the accretion disk blackbody emission is insufficient to explain the broadband AGN spectrum. The total SED with a soft X-ray excess, and a hard X-ray tail, requires additional sources of emission (Kubota & Done 2018). A novel model by Kubota & Done (2018) divides the flow into blackbody emission, warm Comptonization region (the disk), and hard X-ray hot Comptonization component (corona, or a hot material filling the region close to the black hole below the truncation radius). Since the soft X-rays are correlated with the hard X-rays, at least part of the picture consists of reflection or reprocessing of hard X-rays by the disk (Lawrence 2018). This model predicts an increase of variability amplitude (SF_∞) with M_{BH} , and adds an insight that the observed slope is due to changes in accretion rate \dot{m} , explaining that smaller \dot{m} corresponds to highest variability. This qualitatively agrees with the picture that dwindling fuel supply makes the flow more variable. Previous worries about X-ray reprocessing concerned the seemingly insufficient solid angle subtended by the source of the hard X-rays to cause

the observed soft X-ray and optical response. This is addressed by realizing that reprocessing could be taking place in the extended region (Gardner & Done 2017), such as an inflated inner disk (corresponding to warm Comptonizing region in Kubota & Done (2018)), or even the BLR region serving as an additional ‘complex reprocessor’ (McHardy et al. 2018). Also, for Panda et al. (2019a) warm corona helps decrease the dependence of R_{FeII} on f_{Edd} .

Thus while CLAGN may be related to the state-change to ADAF flow (Śniegowska & Czerny 2019) similar to that of XRBs (Noda & Done 2018; Ruan et al. 2019), with cooling and heating fronts (Ross et al. 2018), the more short-timescale variability requires approximately three distinct emission regions (Kubota & Done 2018), with extended reprocessor (diffuse, hot, puffed-up inner disk, and BLR - McHardy et al. 2018), that reverberates the rapid hard X-ray variability in soft X-rays to optical via UV (Fausnaugh et al. 2018). Some emission (especially soft X-rays) seems to require the warm Comptonizing corona Kubota & Done (2018). The warm corona, coupled with metallicity changes, and variation in turbulence level and cloud density, also helps explain the Quasar Main Sequence in the optical (Panda et al. 2019a,b). Finally, the Kubota & Done (2018) model, apart from being consistent with other mechanisms (McHardy et al. 2018; Panda et al. 2019a; Śniegowska & Czerny 2019; Lawrence 2018; Ross et al. 2018; Ruan et al. 2019), explains the observed correlation of variability amplitude with black hole mass as corresponding to variations in mass accretion rate.

7. SUMMARY AND CONCLUSIONS

We model ~ 9000 Stripe82 quasars as the Damped Random Walk (DRW) model with Gaussian Processes implemented in *celerite*. We show that by extending the SDSS light curves with PS1 data we can improve on the recovery of the DRW parameters: characteristic timescale τ and asymptotic variability amplitude SF_{∞} . We find that these correlate with black hole mass M_{BH} and absolute i-band magnitude M_i , with τ more dependent on M_i and less on M_{BH} than in M10. SF_{∞} is less strongly driven by M_i and M_{BH} than M10 found, and has a stronger, almost inverse, dependence on the Eddington ratio f_{Edd} . This is consistent with lower mass accretion rate corresponding to higher variability, so that when the supply of fuel decreases, the flow becomes less stable, more clumpy, more inhomogeneous. This is also consistent with the X-ray reprocessing model, whereby the hard X-ray variability of the inner disk is reflected/reprocessed by the extended warm Comptonization region (inflated disk), and perhaps a complex

reprocessor, including the clouds of the broad line region. Changes on recovered timescales are too fast to be driven by changes in disk viscosity, or thermal front propagation alone - thermal or dynamical timescale of response to the changes in X-ray emission seems most consistent with our results.

More data extending the light curves would help improve the fit coefficients, decreasing the scatter in observed correlations. Given that the uncertainty in black hole mass is one of the biggest sources of error, better measurements of quasar properties would be of high utility. This will be possible by the upcoming AGN reverberation mapping campaigns (SDSS-V Black Hole Mapper, Kollmeier et al. 2017), providing better calibration for line width-based methods of estimating black hole masses. All quasars in this study were spectroscopically confirmed, but some spectra had low signal-to-noise, resulting in higher likelihood of incorrect redshift measurement. Better spectroscopy and follow up of S82 quasars, afforded by SDSS-V panoptic spectroscopy, would not only help improve on the spectrum-based properties (redshift, absolute magnitude, black hole masses), but also allow to study spectral changes, and further new CL AGN discoveries.

If this study were to be expanded onto a sample of quasars with good photometry over sufficiently long baselines, but lacking spectral information, the required physical information on quasars could be obtained by indirect methods of estimating the coarse spectral information from broad-band photometry. This would benefit from better catalogs of existing spectroscopically-confirmed quasars to improve the calibration, as well as better methods of estimating the redshift based on photometry alone (photo-z).

This will be possible in short term with the ZTF, and in the long term with LSST. Occasional coverage adding few epochs to some quasars may be possible with other surveys (eg. TESS), but to improve the statistics an entire sample of S82 quasars would require longer baselines.

8. ACKNOWLEDGEMENTS

The Pan-STARRS1 Surveys (PS1) and the PS1 public science archive have been made possible through contributions by the Institute for Astronomy, the University of Hawaii, the Pan-STARRS Project Office, the Max-Planck Society and its participating institutes, the Max Planck Institute for Astronomy, Heidelberg and the Max Planck Institute for Extraterrestrial Physics, Garching, The Johns Hopkins University, Durham University, the University of Edinburgh, the Queen’s University Belfast, the Harvard-Smithsonian Center for Astrophysics, the

Las Cumbres Observatory Global Telescope Network Incorporated, the National Central University of Taiwan, the Space Telescope Science Institute, the National Aeronautics and Space Administration under Grant No. NNX08AR22G issued through the Planetary Science Division of the NASA Science Mission Directorate, the National Science Foundation Grant No. AST-1238877, the University of Maryland, Eotvos Lorand University (ELTE), the Los Alamos National Laboratory, and the Gordon and Betty Moore Foundation.

Funding for the Sloan Digital Sky Survey IV has been provided by the Alfred P. Sloan Foundation, the U.S. Department of Energy Office of Science, and the Participating Institutions. SDSS-IV acknowledges support and resources from the Center for High-Performance Computing at the University of Utah. The SDSS web site is www.sdss.org.

SDSS-IV is managed by the Astrophysical Research Consortium for the Participating Institutions of the SDSS Collaboration including the Brazilian Participation Group, the Carnegie Institution for Science, Carnegie Mellon University, the Chilean Participation Group, the French Participation Group, Harvard-Smithsonian Center for Astrophysics, Instituto de Astrofísica de Canarias, The Johns Hopkins University, Kavli Institute for the Physics and Mathematics of the Universe (IPMU) / University of Tokyo, the Korean Participation Group, Lawrence Berkeley National Laboratory, Leibniz Institut für Astrophysik Potsdam (AIP), Max-Planck-Institut für Astronomie (MPIA Heidelberg), Max-Planck-Institut für Astrophysik (MPA Garching), Max-Planck-Institut für Extraterrestrische

Physik (MPE), National Astronomical Observatories of China, New Mexico State University, New York University, University of Notre Dame, Observatório Nacional / MCTI, The Ohio State University, Pennsylvania State University, Shanghai Astronomical Observatory, United Kingdom Participation Group, Universidad Nacional Autónoma de México, University of Arizona, University of Colorado Boulder, University of Oxford, University of Portsmouth, University of Utah, University of Virginia, University of Washington, University of Wisconsin, Vanderbilt University, and Yale University.

The CSS survey is funded by the National Aeronautics and Space Administration under Grant No. NNG05GF22G issued through the Science Mission Directorate Near-Earth Objects Observations Program. The CRTS survey is supported by the U.S. National Science Foundation under grants AST-0909182.

Based on observations obtained with the Samuel Oschin 48-inch Telescope at the Palomar Observatory as part of the Zwicky Transient Facility project. ZTF is supported by the National Science Foundation under Grant No. AST-1440341 and a collaboration including Caltech, IPAC, the Weizmann Institute for Science, the Oskar Klein Center at Stockholm University, the University of Maryland, the University of Washington, Deutsches Elektronen-Synchrotron and Humboldt University, Los Alamos National Laboratories, the TANGO Consortium of Taiwan, the University of Wisconsin at Milwaukee, and Lawrence Berkeley National Laboratories. Operations are conducted by COO, IPAC, and UW.

APPENDIX

A. MEASURING BLACK HOLE PROPERTIES

It is difficult to measure the mass of black holes living in the centers of active galaxies, even provided a detailed spectrum. The most common approach to estimate black hole masses in AGN is to assume that the broad-line region (BLR) is virialized:

$$M_{BH} = f \frac{R\Delta V^2}{G} = f M_{vir} \quad (A1)$$

where f is a constant of order unity, R is the size of the BLR (estimated from emission-line lag Δt as $R = c\Delta t$), ΔV is virial velocity, G gravitational constant (Shen et al. 2008). From reverberation mapping studies (eg. Shen et al. 2018) we know that continuum luminosity L is related to the size of the BLR region as $R \propto L^\gamma$ (Vestergaard & Peterson 2006), with γ very close to 1/2 (eg. Bentz et al. 2009 finds from RM studies $\gamma = 0.519 \pm 0.06$). Thus we find that $R\Delta V^2 \propto L^\gamma \Delta V^2 \equiv \mu$. The virial velocity ΔV is usually estimated from the width of the broad emission lines (or line dispersion). In the absence of a quasar spectrum, there are alternative methods using a conversion of the broad-band photometry into monochromatic fluxes in the vicinity of reverberating lines (eg. Kozłowski 2015, used in Kozłowski 2017 to estimate black hole mass for 280 000 AGN). Depending on the redshift, different rest-frame calibrated emission lines shift into the observed passband: broad H α at 6562Å, H β at 5100Å, Mg II at 3000Å, and C IV at 1350Å (see Fig.7 in Shen et al. 2018, and Vestergaard 2002). Some authors even consider separately C IV-based and

Mg II-based black hole mass estimates. We refer the reader to Shen et al. (2008) who in detail describes various biases and inherent assumptions of virial black hole mass measurements.

Another important quasar property - bolometric luminosity, is most often estimated from the absolute i-band magnitude, M_i (see Shen et al. 2008, Fig.2). M_i is derived from the observed i-band magnitude, by correcting for Galactic extinction, and correcting for the fact that at different redshifts different portions of the spectral energy distribution are observed by the telescope filter bandpass. The latter, known as K-correction $K(z)$ (Oke & Sandage 1968), is defined as $m_{intrinsic} = m_{observed} - K(z)$. In the early 2000's the common approach was to K-correct to redshift 0, but as (Richards et al. 2006) pointed out, since the distribution of quasars peaks at redshift 2, for most quasars correcting to the redshift of 0 required shifting the observed spectrum into the far infrared. Moreover, the procedure was to correct separately for the continuum and emission line contributions, assuming a particular spectral shape (eg. power law $f_\nu \propto \nu^\alpha$, with $\alpha = -0.5$ - see Schneider et al. 2010; Vanden Berk et al. 2001; Richards et al. 2006). This introduces a larger error for $K(z=0)$ than for $K(z=2)$ if the assumed spectral shape $\alpha = -0.5$ is far from the real spectral index. In early 2010's, after Richards et al. 2006; Wisotzki 2000; Blanton et al. 2003, the practice started shifting towards K-correcting to redshift 2, and including custom quasar spectral shapes, as reflected by the content of Shen et al. (2011) quasar catalog. Thus in this study we use the absolute i-band magnitude K-corrected to $z=2$: $M_i(z=2)$.

These methods were used to create catalogs of quasar properties derived from spectra. Since quasars are variable at ~ 0.2 mag level, the ideal is to use a single-epoch calibrated spectrum to estimate the continuum luminosity, and find virial black hole masses using relationships based on the monochromatic fluxes and broad line widths described above. A glance at the available quasar catalogs reveals that, given any SDSS data release, there is indeed first a catalog of basic quasar properties (redshift and photometry - eg. Schneider et al. 2007, 2010), and more detailed catalogs containing black hole masses and bolometric luminosities follow (eg. Shen et al. 2008, 2011). More recently, once SDSS DR12 Quasar Catalog (Pâris et al. 2017) was released, Kozłowski, Szymon 2017 followed using SDSS photometry as a proxy for monochromatic luminosities. Chen et al. (2018) added a detailed analysis of continuum luminosities in the $H\alpha$, $H\beta$ regions for low-redshift quasars. Using the spectra from Chinese LAMOST survey Dong et al. (2018) also sought to estimate virial black hole masses, and the results, while consistent with Shen et al. (2011), suffered from the necessity to peg the non-calibrated spectra to the SDSS photometry which was taken a different epoch. Thus even though the SDSS DR12 Quasar Catalog of Pâris et al. (2018) is the most recent, like Pâris et al. (2017) it lacks black hole masses and bolometric luminosities, and there is no recent work that re-analyzed the spectral data. Therefore we use black hole mass estimates and monochromatic luminosities from Shen et al. (2011), based directly on single-epoch spectra.

B. SIMULATED LIGHT CURVES

REFERENCES

- AlSayyad, Y. 2016, PhD thesis, University of Washington.
<http://hdl.handle.net/1773/37020>
- Annis, J., Soares-Santos, M., Strauss, M. A., et al. 2014, ApJ, 794, 120, doi: [10.1088/0004-637X/794/2/120](https://doi.org/10.1088/0004-637X/794/2/120)
- Aranzana, E., K rding, E., Uttley, P., Scaringi, S., & Bloemen, S. 2018, MNRAS, 476, 2501, doi: [10.1093/mnras/sty413](https://doi.org/10.1093/mnras/sty413)
- Babi c, A., Miller, L., Jarvis, M. J., et al. 2007, A&A, 474, 755, doi: [10.1051/0004-6361/20078286](https://doi.org/10.1051/0004-6361/20078286)
- Balbus, S. A. 2003, ARA&A, 41, 555, doi: [10.1146/annurev.astro.41.081401.155207](https://doi.org/10.1146/annurev.astro.41.081401.155207)
- Balbus, S. A., & Hawley, J. F. 1998, Reviews of Modern Physics, 70, 1, doi: [10.1103/RevModPhys.70.1](https://doi.org/10.1103/RevModPhys.70.1)
- Bauer, A., Baltay, C., Coppi, P., et al. 2009, ApJ, 696, 1241, doi: [10.1088/0004-637X/696/2/1241](https://doi.org/10.1088/0004-637X/696/2/1241)
- Bentz, M. C., Peterson, B. M., Netzer, H., Pogge, R. W., & Vestergaard, M. 2009, ApJ, 697, 160, doi: [10.1088/0004-637X/697/1/160](https://doi.org/10.1088/0004-637X/697/1/160)
- Bianchi, S., Piconcelli, E., Chiaberge, M., et al. 2009, ApJ, 695, 781, doi: [10.1088/0004-637X/695/1/781](https://doi.org/10.1088/0004-637X/695/1/781)
- Blanton, M. R., Lin, H., Lupton, R. H., et al. 2003, AJ, 125, 2276, doi: [10.1086/344761](https://doi.org/10.1086/344761)
- Borucki, W. J., Koch, D., Basri, G., et al. 2010, Science, 327, 977, doi: [10.1126/science.1185402](https://doi.org/10.1126/science.1185402)
- Cai, Z.-Y., Wang, J.-X., Gu, W.-M., et al. 2016, ApJ, 826, 7, doi: [10.3847/0004-637X/826/1/7](https://doi.org/10.3847/0004-637X/826/1/7)
- Caplar, N., Lilly, S. J., & Trakhtenbrot, B. 2017, ApJ, 834, 111, doi: [10.3847/1538-4357/834/2/111](https://doi.org/10.3847/1538-4357/834/2/111)
- Chambers, K. C. 2011, in Bulletin of the American Astronomical Society, Vol. 43, American Astronomical Society Meeting Abstracts #218, 113.01

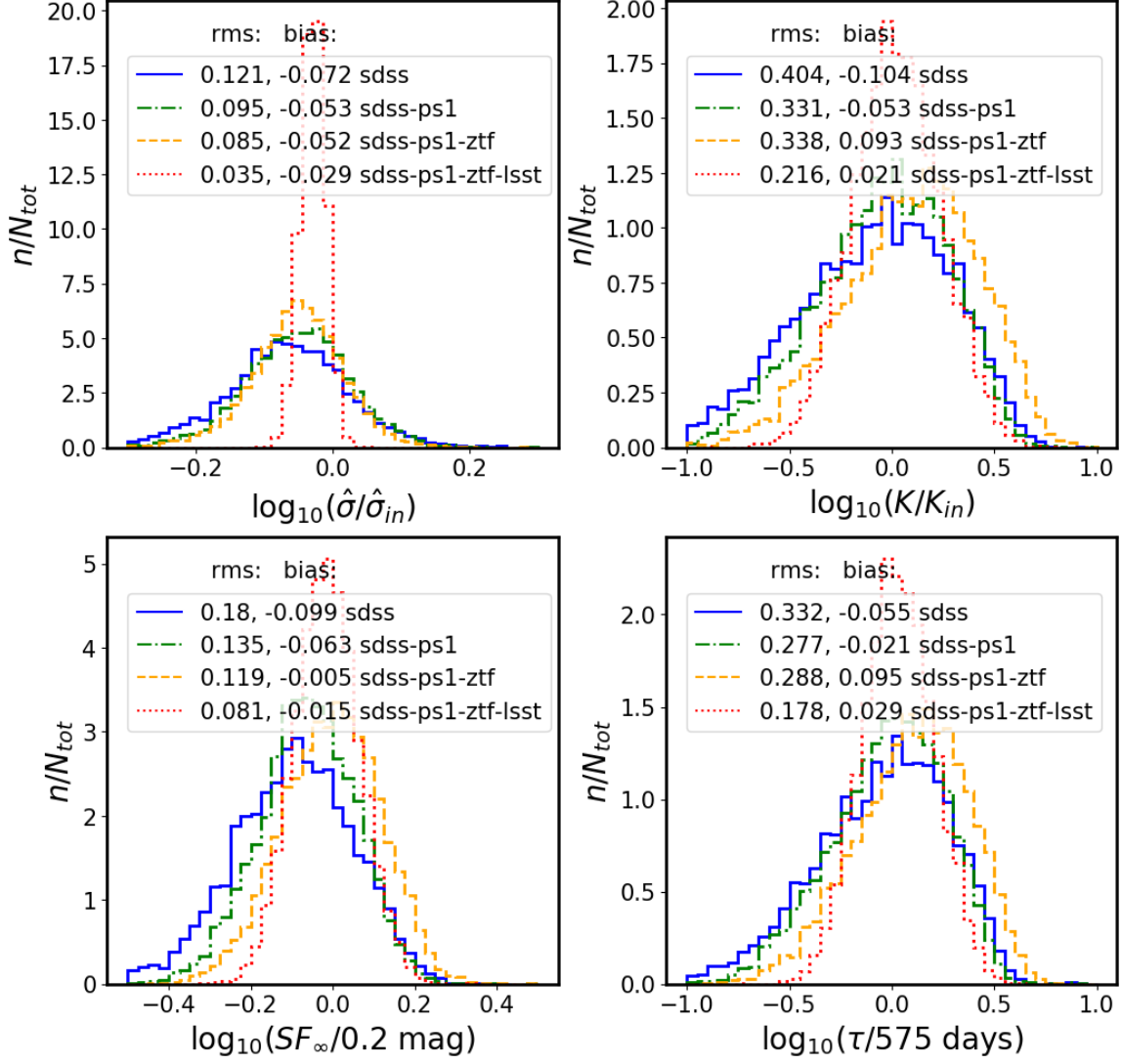


Figure 22. Comparison of retrieved parameters in relation to input parameters, shown as Fig.18 in MacLeod et al. (2011)

Charisi, M., Bartos, I., Haiman, Z., et al. 2016, MNRAS, 463, 2145, doi: [10.1093/mnras/stw1838](https://doi.org/10.1093/mnras/stw1838)

Chen, Z.-F., Pan, D.-S., Pang, T.-T., & Huang, Y. 2018, ApJS, 234, 16, doi: [10.3847/1538-4365/aa9d90](https://doi.org/10.3847/1538-4365/aa9d90)

Czerny, B. 2006, in Astronomical Society of the Pacific Conference Series, Vol. 360, AGN Variability from X-Rays to Radio Waves, ed. C. M. Gaskell, I. M. McHardy, B. M. Peterson, & S. G. Sergeev, 265

Dexter, J., & Agol, E. 2011, ApJL, 727, L24, doi: [10.1088/2041-8205/727/1/L24](https://doi.org/10.1088/2041-8205/727/1/L24)

Dexter, J., & Begelman, M. C. 2019, MNRAS, 483, L17, doi: [10.1093/mnrasl/sly213](https://doi.org/10.1093/mnrasl/sly213)

Dong, X. Y., Wu, X.-B., Ai, Y. L., et al. 2018, AJ, 155, 189, doi: [10.3847/1538-3881/aab5ae](https://doi.org/10.3847/1538-3881/aab5ae)

Drake, A. J., Djorgovski, S. G., Mahabal, A., et al. 2009, ApJ, 696, 870, doi: [10.1088/0004-637X/696/1/870](https://doi.org/10.1088/0004-637X/696/1/870)

Eardley, D. M., & Lightman, A. P. 1975, ApJ, 200, 187, doi: [10.1086/153777](https://doi.org/10.1086/153777)

Edelson, R., Vaughan, S., Malkan, M., et al. 2014, ApJ, 795, 2, doi: [10.1088/0004-637X/795/1/2](https://doi.org/10.1088/0004-637X/795/1/2)

Edelson, R., Gelbord, J. M., Horne, K., et al. 2015, ApJ, 806, 129, doi: [10.1088/0004-637X/806/1/129](https://doi.org/10.1088/0004-637X/806/1/129)

Fausnaugh, M. M., Denney, K. D., Barth, A. J., et al. 2016, ApJ, 821, 56, doi: [10.3847/0004-637X/821/1/56](https://doi.org/10.3847/0004-637X/821/1/56)

Fausnaugh, M. M., Starkey, D. A., Horne, K., et al. 2018, ApJ, 854, 107, doi: [10.3847/1538-4357/aaa2b](https://doi.org/10.3847/1538-4357/aaa2b)

Ferrarese, L., & Merritt, D. 2000, The Astrophysical Journal, 539, L9, doi: [10.1086/312838](https://doi.org/10.1086/312838)

Flewelling, H. 2018, in American Astronomical Society Meeting Abstracts, Vol. 231, American Astronomical Society Meeting Abstracts 231, 436.01

- Foreman-Mackey, D., Agol, E., Angus, R., & Ambikasaran, S. 2017, ArXiv e-prints.
<https://arxiv.org/abs/1703.09710>
- Frank, J., King, A., & Raine, D. J. 2002, *Accretion Power in Astrophysics: Third Edition* (Cambridge University Press), 398
- Frederick, S., Gezari, S., Graham, M. J., et al. 2019, arXiv e-prints, arXiv:1904.10973.
<https://arxiv.org/abs/1904.10973>
- Gardner, E., & Done, C. 2017, *Monthly Notices of the Royal Astronomical Society*, 470, 3591,
 doi: [10.1093/mnras/stx946](https://doi.org/10.1093/mnras/stx946)
- Graham, M. J., Djorgovski, S. G., Stern, D., et al. 2015, *Nature*, 518, 74, doi: [10.1038/nature14143](https://doi.org/10.1038/nature14143)
- Graham, M. J., Ross, N. P., Stern, D., et al. 2019, arXiv e-prints, arXiv:1905.02262.
<https://arxiv.org/abs/1905.02262>
- Grzędzielski, M., Janiuk, A., Czerny, B., & Wu, Q. 2017, *A&A*, 603, A110, doi: [10.1051/0004-6361/201629672](https://doi.org/10.1051/0004-6361/201629672)
- Guo, H., Wang, J., Cai, Z., & Sun, M. 2017, *ApJ*, 847, 132, doi: [10.3847/1538-4357/aa8d71](https://doi.org/10.3847/1538-4357/aa8d71)
- Hameury, J.-M., Viallet, M., & Lasota, J.-P. 2009, *A&A*, 496, 413, doi: [10.1051/0004-6361/200810928](https://doi.org/10.1051/0004-6361/200810928)
- Hernitschek, N., Schlafly, E. F., Sesar, B., et al. 2016, *The Astrophysical Journal*, 817, 73
- Ivezić, Ž., Smith, J. A., Miknaitis, G., et al. 2007, *AJ*, 134, 973, doi: [10.1086/519976](https://doi.org/10.1086/519976)
- Ivezić, Ž., Kahn, S. M., Tyson, J. A., et al. 2019, *ApJ*, 873, 111, doi: [10.3847/1538-4357/ab042c](https://doi.org/10.3847/1538-4357/ab042c)
- Jiang, Y.-F., Davis, S. W., & Stone, J. M. 2016, *ApJ*, 827, 10, doi: [10.3847/0004-637X/827/1/10](https://doi.org/10.3847/0004-637X/827/1/10)
- Kasliwal, V. P., Vogeley, M. S., & Richards, G. T. 2015, *MNRAS*, 451, 4328, doi: [10.1093/mnras/stv1230](https://doi.org/10.1093/mnras/stv1230)
- Kelly, B. C. 2007, *ApJ*, 665, 1489, doi: [10.1086/519947](https://doi.org/10.1086/519947)
- Kelly, B. C., Bechtold, J., & Siemiginowska, A. 2009, *The Astrophysical Journal*, 698, 895
- Kelly, B. C., Becker, A. C., Sobolewska, M., Siemiginowska, A., & Uttley, P. 2014, *ApJ*, 788, 33,
 doi: [10.1088/0004-637X/788/1/33](https://doi.org/10.1088/0004-637X/788/1/33)
- Kelly, B. C., Treu, T., Malkan, M., Pancoast, A., & Woo, J.-H. 2013, *ApJ*, 779, 187,
 doi: [10.1088/0004-637X/779/2/187](https://doi.org/10.1088/0004-637X/779/2/187)
- Kokubo, M. 2015, *MNRAS*, 449, 94,
 doi: [10.1093/mnras/stv241](https://doi.org/10.1093/mnras/stv241)
- Kollmeier, J. A., Zasowski, G., Rix, H.-W., et al. 2017, arXiv e-prints, arXiv:1711.03234.
<https://arxiv.org/abs/1711.03234>
- Kormendy, J., & Ho, L. C. 2013, *ARA&A*, 51, 511,
 doi: [10.1146/annurev-astro-082708-101811](https://doi.org/10.1146/annurev-astro-082708-101811)
- Kozłowski, S. 2015, *AcA*, 65, 251.
<https://arxiv.org/abs/1504.05960>
- Kozłowski, S. 2016, *MNRAS*, 459, 2787,
 doi: [10.1093/mnras/stw819](https://doi.org/10.1093/mnras/stw819)
- Kozłowski, S. 2017, *ApJS*, 228, 9,
 doi: [10.3847/1538-4365/228/1/9](https://doi.org/10.3847/1538-4365/228/1/9)
- Kozłowski, S., Kochanek, C. S., Udalski, A., et al. 2010, *ApJ*, 708, 927
- Kozłowski, Szymon. 2017, *A&A*, 597, A128,
 doi: [10.1051/0004-6361/201629890](https://doi.org/10.1051/0004-6361/201629890)
- Krolik, J. H., Horne, K., Kallman, T. R., et al. 1991, *ApJ*, 371, 541, doi: [10.1086/169918](https://doi.org/10.1086/169918)
- Kubota, A., & Done, C. 2018, *MNRAS*, 480, 1247,
 doi: [10.1093/mnras/sty1890](https://doi.org/10.1093/mnras/sty1890)
- Labita, M., Decarli, R., Treves, A., & Falomo, R. 2009, *MNRAS*, 399, 2099,
 doi: [10.1111/j.1365-2966.2009.15400.x](https://doi.org/10.1111/j.1365-2966.2009.15400.x)
- LaMassa, S. M., Cales, S., Moran, E. C., et al. 2015, *ApJ*, 800, 144, doi: [10.1088/0004-637X/800/2/144](https://doi.org/10.1088/0004-637X/800/2/144)
- Lasota, J.-P. 2016, in *Astrophysics and Space Science Library*, Vol. 440, *Astrophysics of Black Holes: From Fundamental Aspects to Latest Developments*, ed. C. Bambi, 1
- Lawrence, A. 2018, *Nature Astronomy*, 2, 102,
 doi: [10.1038/s41550-017-0372-1](https://doi.org/10.1038/s41550-017-0372-1)
- Li, Z., McGreer, I. D., Wu, X.-B., Fan, X., & Yang, Q. 2018, *ApJ*, 861, 6, doi: [10.3847/1538-4357/aac6ce](https://doi.org/10.3847/1538-4357/aac6ce)
- Lira, P., Arévalo, P., Uttley, P., McHardy, I. M. M., & Videla, L. 2015, *MNRAS*, 454, 368,
 doi: [10.1093/mnras/stv1945](https://doi.org/10.1093/mnras/stv1945)
- MacLeod, C. L., Ivezić, Ž., Kochanek, C. S., et al. 2010, *The Astrophysical Journal*, 721, 1014
- MacLeod, C. L., Brooks, K., Ivezić, Ž., et al. 2011, *The Astrophysical Journal*, 728, 26
- MacLeod, C. L., Ivezić, Ž., Sesar, B., et al. 2012, *The Astrophysical Journal*, 753, 106
- MacLeod, C. L., Green, P. J., Anderson, S. F., et al. 2019, *ApJ*, 874, 8, doi: [10.3847/1538-4357/ab05e2](https://doi.org/10.3847/1538-4357/ab05e2)
- Marchese, E., Baito, V., Della Ceca, R., Caccianiga, A., & Severgnini, P. 2012, *Monthly Notices of the Royal Astronomical Society*, 421, 1803,
 doi: [10.1111/j.1365-2966.2012.20445.x](https://doi.org/10.1111/j.1365-2966.2012.20445.x)
- Marziani, P., Dultzin, D., Sulentic, J. W., et al. 2018, *Frontiers in Astronomy and Space Sciences*, 5, 6,
 doi: [10.3389/fspas.2018.00006](https://doi.org/10.3389/fspas.2018.00006)
- McGreer, I. D., Fan, X., Jiang, L., & Cai, Z. 2018, *AJ*, 155, 131, doi: [10.3847/1538-3881/aaaab4](https://doi.org/10.3847/1538-3881/aaaab4)
- McGreer, I. D., Jiang, L., Fan, X., et al. 2013, *ApJ*, 768, 105, doi: [10.1088/0004-637X/768/2/105](https://doi.org/10.1088/0004-637X/768/2/105)

- McHardy, I. M., Connolly, S. D., Horne, K., et al. 2018, MNRAS, 480, 2881, doi: [10.1093/mnras/sty1983](https://doi.org/10.1093/mnras/sty1983)
- McLure, R. J., & Dunlop, J. S. 2004, MNRAS, 352, 1390, doi: [10.1111/j.1365-2966.2004.08034.x](https://doi.org/10.1111/j.1365-2966.2004.08034.x)
- Mushotzky, R. F., Edelson, R., Baumgartner, W., & Gandhi, P. 2011, The Astrophysical Journal, 743, L12, doi: [10.1088/2041-8205/743/1/L12](https://doi.org/10.1088/2041-8205/743/1/L12)
- Netzer, H. 2013, The Physics and Evolution of Active Galactic Nuclei (Cambridge University Press)
- Noda, H., & Done, C. 2018, MNRAS, 480, 3898, doi: [10.1093/mnras/sty2032](https://doi.org/10.1093/mnras/sty2032)
- Oke, J. B., & Sandage, A. 1968, ApJ, 154, 21, doi: [10.1086/149737](https://doi.org/10.1086/149737)
- Palanque-Delabrouille, N., Magneville, C., Yèche, C., et al. 2013, A&A, 551, A29, doi: [10.1051/0004-6361/201220379](https://doi.org/10.1051/0004-6361/201220379)
- Panda, S., Czerny, B., Done, C., & Kubota, A. 2019a, ApJ, 875, 133, doi: [10.3847/1538-4357/ab11cb](https://doi.org/10.3847/1538-4357/ab11cb)
- Panda, S., Marziani, P., & Czerny, B. 2019b, arXiv e-prints, arXiv:1905.01729. <https://arxiv.org/abs/1905.01729>
- Pâris, I., Petitjean, P., Ross, N. P., et al. 2017, A&A, 597, A79, doi: [10.1051/0004-6361/201527999](https://doi.org/10.1051/0004-6361/201527999)
- Pâris, I., Petitjean, P., Aubourg, É., et al. 2018, A&A, 613, A51, doi: [10.1051/0004-6361/201732445](https://doi.org/10.1051/0004-6361/201732445)
- Rakshit, S., & Stalin, C. S. 2017, ApJ, 842, 96, doi: [10.3847/1538-4357/aa72f4](https://doi.org/10.3847/1538-4357/aa72f4)
- Rasmussen, C. E., & Williams, C. K. I. 2006, Gaussian Processes for Machine Learning (Cambridge, MA: MIT Press)
- Rau, A., Kulkarni, S. R., Law, N. M., et al. 2009, PASP, 121, 1334, doi: [10.1086/605911](https://doi.org/10.1086/605911)
- Richards, G. T., Strauss, M. A., Fan, X., et al. 2006, AJ, 131, 2766, doi: [10.1086/503559](https://doi.org/10.1086/503559)
- Risaliti, G., Miniutti, G., Elvis, M., et al. 2009, The Astrophysical Journal, 696, 160, doi: [10.1088/0004-637x/696/1/160](https://doi.org/10.1088/0004-637x/696/1/160)
- Ross, N. P., McGreer, I. D., White, M., et al. 2013, ApJ, 773, doi: [10.1088/0004-637X/773/1/14](https://doi.org/10.1088/0004-637X/773/1/14)
- Ross, N. P., Ford, K. E. S., Graham, M., et al. 2018, MNRAS, 480, 4468, doi: [10.1093/mnras/sty2002](https://doi.org/10.1093/mnras/sty2002)
- Ruan, J. J., Anderson, S. F., Dexter, J., & Agol, E. 2014, The Astrophysical Journal, 783, 105, doi: [10.1088/0004-637x/783/2/105](https://doi.org/10.1088/0004-637x/783/2/105)
- Ruan, J. J., Anderson, S. F., Eracleous, M., et al. 2019, arXiv e-prints, arXiv:1903.02553. <https://arxiv.org/abs/1903.02553>
- Rumbaugh, N., Shen, Y., Morganson, E., et al. 2018, ApJ, 854, 160, doi: [10.3847/1538-4357/aaa9b6](https://doi.org/10.3847/1538-4357/aaa9b6)
- Rybicki, G. B., & Press, W. H. 1992, ApJ, 398, 169, doi: [10.1086/171845](https://doi.org/10.1086/171845)
- Sánchez-Sáez, P., Lira, P., Mejía-Restrepo, J., et al. 2018, ApJ, 864, 87, doi: [10.3847/1538-4357/aad7f9](https://doi.org/10.3847/1538-4357/aad7f9)
- Schmidt, K. B., Marshall, P. J., Rix, H.-W., et al. 2010, ApJ, 714, 1194, doi: [10.1088/0004-637X/714/2/1194](https://doi.org/10.1088/0004-637X/714/2/1194)
- Schneider, D. P., Hall, P. B., Richards, G. T., et al. 2007, AJ, 134, 102, doi: [10.1086/518474](https://doi.org/10.1086/518474)
- . 2008, VizieR Online Data Catalog, 7252
- Schneider, D. P., Richards, G. T., Hall, P. B., et al. 2010, AJ, 139, 2360, doi: [10.1088/0004-6256/139/6/2360](https://doi.org/10.1088/0004-6256/139/6/2360)
- Sesar, B., Ivezić, Ž., Lupton, R. H., et al. 2007, AJ, 134, 2236
- Shakura, N. I., & Sunyaev, R. A. 1973, A&A, 24, 337
- Shen, Y., Greene, J. E., Strauss, M. A., Richards, G. T., & Schneider, D. P. 2008, ApJ, 680, 169, doi: [10.1086/587475](https://doi.org/10.1086/587475)
- Shen, Y., & Ho, L. C. 2014, Nature, 513, 210, doi: [10.1038/nature13712](https://doi.org/10.1038/nature13712)
- Shen, Y., Richards, G. T., Strauss, M. A., et al. 2011, ApJS, 194, 45, doi: [10.1088/0067-0049/194/2/45](https://doi.org/10.1088/0067-0049/194/2/45)
- Shen, Y., Hall, P. B., Horne, K., et al. 2018, arXiv e-prints, arXiv:1810.01447. <https://arxiv.org/abs/1810.01447>
- Simm, T., Salvato, M., Saglia, R., et al. 2016, A&A, 585, A129, doi: [10.1051/0004-6361/201527353](https://doi.org/10.1051/0004-6361/201527353)
- Smith, K. L., Mushotzky, R. F., Boyd, P. T., et al. 2018, ApJ, 857, 141, doi: [10.3847/1538-4357/aab88d](https://doi.org/10.3847/1538-4357/aab88d)
- Śniegowska, M., & Czerny, B. 2019, arXiv e-prints, arXiv:1904.06767. <https://arxiv.org/abs/1904.06767>
- Stern, D., McKernan, B., Graham, M. J., et al. 2018, ApJ, 864, 27, doi: [10.3847/1538-4357/aac726](https://doi.org/10.3847/1538-4357/aac726)
- Suberlak, K., Ivezić, Ž., MacLeod, C. L., Graham, M., & Sesar, B. 2017, MNRAS, 472, 4870, doi: [10.1093/mnras/stx2310](https://doi.org/10.1093/mnras/stx2310)
- Sun, J., & Shen, Y. 2015, ApJL, 804, L15, doi: [10.1088/2041-8205/804/1/L15](https://doi.org/10.1088/2041-8205/804/1/L15)
- Sun, M., Xue, Y., Wang, J., Cai, Z., & Guo, H. 2018, ApJ, 866, 74, doi: [10.3847/1538-4357/aae208](https://doi.org/10.3847/1538-4357/aae208)
- Vanden Berk, D. E., Richards, G. T., Bauer, A., et al. 2001, AJ, 122, 549, doi: [10.1086/321167](https://doi.org/10.1086/321167)
- Vestergaard, M. 2002, ApJ, 571, 733, doi: [10.1086/340045](https://doi.org/10.1086/340045)
- Vestergaard, M., & Peterson, B. M. 2006, ApJ, 641, 689, doi: [10.1086/500572](https://doi.org/10.1086/500572)
- Wang, T., Brinkmann, W., & Bergeron, J. 1996, A&A, 309, 81
- Wisotzki, L. 2000, A&A, 353, 861
- Yang, J., Fan, X., Wu, X.-B., et al. 2017, AJ, 153, 184, doi: [10.3847/1538-3881/aa6577](https://doi.org/10.3847/1538-3881/aa6577)
- Zhu, F.-F., Wang, J.-X., Cai, Z.-Y., et al. 2018, The Astrophysical Journal, 860, 29, doi: [10.3847/1538-4357/aac2d7](https://doi.org/10.3847/1538-4357/aac2d7)
- Zu, Y., Kochanek, C. S., Kozłowski, S., & Udalski, A. 2013, ApJ, 765, 106, doi: [10.1088/0004-637X/765/2/106](https://doi.org/10.1088/0004-637X/765/2/106)

Zu, Y., Kochanek, C. S., & Peterson, B. M. 2011, ApJ, 735,
80